ORIGINAL RESEARCH **Open access**

Optimal-Control-Based Reference Generation for Energy-Efficient Quadrotor Flight

Linus Chen[1*], Yuki Sato[2], Olivia Harris[1], Takeshi Mori[3]

Abstract

Driven by the restricted battery endurance of multi-rotor unmanned aerial vehicles (UAVs), the present work examined hierarchical real-time control of UAVs combined with the synthesis of energy-optimal reference trajectories. The aim was to devise a reference generator and controller rooted in optimal-control principles that would deliver energy usage approaching the optimum while demanding less computational effort. Initially, a least-squares estimation (LSE) algorithm was applied to determine the parameters of the UAV's mathematical representation. Next, by incorporating a detailed electrical characterization of the brushless DC motors and considering rest-to-rest maneuvers, explicit criteria for calculating the optimal mission duration and constructing 'energetic trajectories' were obtained. These criteria emerged from scrutinizing the optimal-control policy outcomes that reduced consumption over an extensive set of simulations. Afterward, a hierarchical controller followed the prescribed, sub-optimal energetic trajectories. Numerical experiments assessed outcomes for trajectory following, the energy performance metric, and battery state of charge (SOC). A co-simulation setup integrating commercial software tools—Simcenter Amesim for the UAV's physical representation and Matlab-Simulink—performed the numerical simulations of the devised controller.

Keywords UAV control, Energetic reference generator, Optimal control, Hierarchical control, Energy consumption

*Correspondence:
Linus Chen
linus.chen@ucdavis.edu
[1] Department of Artificial Intelligence for Strawberry and Lettuce Yield Forecasting in Controlled Environments, School of Agriculture, University of California, Davis, Davis, United States
[2] Department of Intelligent Robotic Harvesting Systems, Graduate School of Agriculture, University of Tokyo, Tokyo, Japan
[3] Department of Machine Learning for Nutrient Solution Optimization, Faculty of Agriculture, Kyoto University, Kyoto, Japan

Introduction

Context

Over the past several years, UAVs have attracted significant interest across a broad range of sectors, including academics, police forces, delivery companies, search-and-rescue units, and agricultural firms. Their flexible use cases have spurred deep research and investigation throughout these heterogeneous industries. Additionally, UAVs are moving beyond their original purpose in sensing operations [1, 2] to fulfill an essential role in operational duties. This transition underscores the growing relevance of UAVs, not only for information acquisition but also for tangible implementation activities. A developing field of inquiry involves coupling manipulators with UAVs, empowering them to perform actions such as valve manipulation and picking up and depositing objects. This multidisciplinary strategy has the potential to enhance the adaptability of UAVs across a range of practical scenarios. Scholars underscore that compact UAVs, in addition to their manipulation capabilities, have considerable potential to advance remote sensing research. The nimbleness and ease of deployment of small UAVs could markedly enhance information gathering and interpretation in isolated, harsh environments. In the upcoming years, a pronounced rise in experimental UAV applications is foreseen.

This is an open access article distributed under the terms of the Creative Commons Attribution-NonCommercial-ShareAlike 4.0 International License (CC BY-NC-SA 4.0), which permits non-commercial use, distribution, reproduction, and adaptation in any medium or format, provided that appropriate credit is given to the original author(s) and source, a link to the license is provided, and any changes made are indicated. Adapted material must be distributed under the same license.

© 2023 The Author(s). | Published by Agro Intelligence Research Press

Illustrations of this mounting enthusiasm include a Canadian business commencing drone-based freight deliveries [3], an Australian enterprise rolling out drone-delivered coffee [4], and fruitful tests using drones for the carriage of organ transplants [5]. Moreover, UAVs are increasingly deployed to convey flexible linear items, such as hoses and merchandise [6, 7], and Swiss Post has used UAVs to deliver medical specimens, radically slashing travel time from 45 minutes by road to only a handful of minutes in the air [7]. What is more, a recent study found that UAV deliveries could help reduce greenhouse gas emissions in the cargo sector [8]. This observation spotlights the ecological advantages that trailblazing UAV deployments could supply to the transportation domain.

The surging appetite for UAV deployments highlights the imperative to boost their effectiveness, as noted by Jensen-Nau *et al.* [9]. A principal obstacle across diverse applications is the limited energy storage capacity of batteries or alternative power sources, even when employing hybrid setups. At present, off-the-shelf battery-operated multirotors deliver an average flight span of 15 to 45 min, harshly limiting their real-world usefulness. This shortcoming stresses the urgent demand for capability upgrades across multiple dimensions of UAV technology. Besides, the energy reservoir has to be allocated among numerous uses, for instance, the power-hungry processes of video and image analytics routinely deployed on drones [10]. To address this challenge and improve overall efficiency, sustained efforts are focusing on advancing energy sources, making drone components lighter, refining energy use, and refining flight trajectories. Salient tactics include reducing UAV mass via carbon-fiber structures and clever designs with superior energy density, along with gains in power-to-weight ratio. These schemes are jointly helping render UAV platforms more capable and productive.

Relevant and related work

Power draw in multirotors is a pivotal factor, given that they rely on batteries with finite lifetimes. The elevated power consumption fundamentally stems from the motors spinning the rotors to generate the thrust required for UAV flight [11]. The electrical energy drawn by these motors depends on the thrust requirements and accounts for losses due to heat, friction, and the aggregate efficiency of the propulsion train. This efficiency measure accounts for losses in both motors and electronic speed controllers, thereby shaping the overall power consumption of multirotor UAVs. Methods to fine-tune power draw and lift efficiency are fundamental for extending flight duration and improving the overall performance of these unmanned platforms. Lately, a wide range of research efforts has been pursued to address energy-conservation challenges in UAVs. This spans explorations into the architecture of automated battery recharge/exchange systems, aimed at improving power-handling efficiency. Alongside these endeavors, efforts have focused on refining trajectories and control inputs to curtail energy use during UAV operations. These varied strategies reflect the steady resolve to craft inventive solutions that can promote energy conservation, thereby broadening the functional reach of unmanned aerial vehicles.

The study by Swieringa *et al.* [12] presented a battery-swap apparatus to efficiently manage the resource and condition-monitoring systems of UAVs while reducing operator burden. This arrangement not only permits the detachment, recharging, and fitting of batteries but also embeds an online algorithm that coordinates the simultaneous replenishment of multiple UAVs. The algorithm determines when a craft requires refueling and ensures a pinpoint touchdown on the battery-swap unit's landing zone. A further contribution by Leonard *et al.* [13] outlined the conception, trialing, and assembly of a self-sufficient terrestrial charging base purpose-built for battery-powered quadrotor helicopters. Moreover, inquiries in the same field have explored advanced methods of energy replenishment for multi-rotors, for instance, wireless charging [14, 15]. In tandem with recharging innovations, investigative efforts have zeroed in on two primary avenues for tackling energy limitations in conveyance: improving the design phase of airborne transport and reducing energy expenditure through streamlined operational scheduling. These breakthroughs aim to jointly improve the holistic energy efficiency and self-reliance of UAVs across a wide range of applications.

Energy savings in the design phase of UAVs can be achieved through multiple tactics, one of which focuses on reducing the mass the UAV must carry. For compact UAVs, where the battery alone may account for as much as 50% of the overall weight [16], shedding excess payload mass is vital for achieving a better energy balance. Operating at an optimal weight can boost UAV endurance and broader flight performance [17]. Furthermore, hybrid configurations, such as the one

© 2023 The Author(s). | Published by Agro Intelligence Research Press

proposed by Morton and Papanikolopoulos [18], enable UAVs to move on the ground when aerial travel is unnecessary, thereby aiding energy conservation. The second avenue toward energy savings entails efficient motion scheduling, which is the core focus of the investigation outlined in this article. This strategy involves selecting, from a set of candidate paths generated by a route planner, the one that incurs the least energy expenditure, as demonstrated by Economou *et al.* [19]. The technique described by Economou *et al.* [19] used offline energy-optimal route planning based on the Dijkstra algorithm, providing a systematic means to improve UAV energy performance during operations.

Regarding the regulation of minimal-energy trajectories, Carvajal *et al.* [20] put forward a stable path-adherence controller derived from a reduced kinematic representation of a quadrotor. Across multiple trials, they demonstrated the robust performance of this controller under both steady and fluctuating target speed profiles, the latter determined by the predefined route's geometric constraints. In addition, substantial research has focused on the use of real-time dynamic programming (RTDP) methods for drones, as underscored by Mohiuddin *et al.* [21]. The optimization scheme developed in that study drew inspiration from a dynamic, real-time programming framework originally proposed by Levermore *et al.* [22], which was designed for velocity optimization to reduce energy consumption in cars. These developments have furthered the ongoing push to develop effective, adaptive UAV control methodologies, especially in the realm of energy-conscious path generation.

Rossi *et al.* [23] proposed a quadratic programming formulation for constructing trajectories for aerial manipulators. While successful, a notable limitation emerged regarding computational load and energy consumption, most acutely during onboard execution. Along parallel lines, Kreciglowa *et al.* [24] probed the identification of the optimal trajectory for a quadrotor aerial platform moving between two hovering states through the lens of energy expenditure. Three smooth-trajectory categories were examined: minimum snap, minimum jerk, and minimum acceleration. Yet the minimization task in that study omitted a dedicated model and provided no estimate of the optimal mission duration, thereby setting it apart from the framework advanced in the present manuscript.

In a recent contribution [25], a technique was proposed to construct a dynamic representation capable of forecasting energy consumption in quadrotors. This model was purpose-built to dissect the energy performance of the quadrotor across varying flight maneuvers. Within the fixed-wing UAV arena, Chodnicki *et al.* [26] delved into an energy-saving control strategy reliant on deriving flight paths via a hexagonal lattice. This exploration added to the ongoing drive to boost the energy economy and the self-sufficiency of unmanned aircraft platforms through sophisticated regulatory frameworks. In the study by Morbidi *et al.* [27], trajectories of minimal energy were determined for a quadrotor linking start and end states by tackling an optimal control formulation grounded in the UAV model. Concurrently, a path minimizing time and/or control effort was determined by solving a corresponding optimal-control formulation. Nonetheless, the technique outlined in this investigation was conducted offline, and its lack of feedback rendered it unworkable for certain use cases. A conceivable remedy lies in periodic invocation, recalculating optimal trajectory setpoints with feedback. Even so, such a tactic, though less demanding than dynamic programming, still consumes appreciable energy and requires hardware with high-grade processing capacity.

Over the past few years, numerous investigations have focused on reference signal construction, recognizing its impact on energy consumption. In Zhou *et al.* [28], the authors explored a trajectory-scheduling algorithm for a UAV that accounted for constraints on positioning precision. A separate inquiry by Yu *et al.* [29] cast trajectory generation as a quadratic-programming task with linear constraints, explicitly confronting the difficulty of executing aggressive flight routines with quadrotors. Beyond that, Schacht-Rodriguez *et al.* [30] proposed a path-planning generation algorithm that accounted for the progression of battery behavior. This tactic entails computing the battery state of health (SoH) through deterioration models and framing the path-planning algorithm as a multi-objective optimization challenge. The aim is to pinpoint a viable path between waypoints that jointly minimizes energy expenditure and mission duration while accommodating shifts in the battery SoH. These inquiries have jointly advanced the collective endeavor to refine energy-conscious reference generation for UAVs. In Wu *et al.* [31], seeking to raise the effectiveness of UAVs in transmission-tower inspection, a UAV transmission-tower-inspection energy-consumption representation was put forward to address the prior absence of a precise energy-consumption-estimation method for such tasks, and the optimal energy-use path for

© 2023 The Author(s). | Published by Agro Intelligence Research Press

UAV transmission-tower inspection was constructed in conjunction with a simulated annealing algorithm. A methodology for capturing the complete translational dynamics of a quadrotor UAV via a feedforward neural network was advanced by Jiang *et al.* [32], which was then employed as the predictive element in a model predictive controller (MPC) for exact position regulation. Finally, the objective of Giernacki [33] was to illuminate the challenge of sculpting control inputs for energy-optimal flight. The construction of a UAV autonomous regulation system incorporating a brain-emotion learning-based intelligent controller (BELBIC) is detailed.

Original contributions and organization

It stands as a legitimate observation that, across numerous published efforts, the twin considerations of energy thriftiness and computational practicality have seldom been examined together in depth. While framing the task as an optimal control problem encompassing varied objectives is indispensable for energy refinement, applied concerns tied to computational load and long-term cost viability at the deployment stage are routinely sidelined. Our investigative stance, which simultaneously weighs both energy and computational dimensions, provides a distinctive, all-encompassing perspective vital for confronting real-world deployments. This twofold viewpoint is poised to make a meaningful addition to a more complete grasp and resolution of the difficulties inherent in refining UAV functions.

The contribution of our study, as characterized, lies in providing rules for optimal mission duration and trajectory synthesis for drones that are not merely energy-sparing but also computationally feasible. The stress on calculational simplicity and closeness to the true optimum is especially significant, as it eases the rollout of real-time hierarchical regulation with modest computational prerequisites. This orientation addresses the pragmatic hurdles of fielding UAVs in authentic settings, where both energy thrift and processing efficiency are decisive factors. The present work has the potential to leave a substantial imprint on the domain by providing a workable and powerful solution to streamline UAV operations across both energy consumption and computational load. The procedure adopted in our investigation is worthy of note, commencing with the determination of unidentified quadrotor parameters via the least-squares method applied to experimental datasets. From there, the extraction of rules for mission timing and trajectory construction that sit near the energy-optimal mark embodies an original and pragmatic methodology. The influence taken from Bianchi *et al.* [34], even though its roots lie in the automotive sphere, reflects inventive reasoning in porting such approaches to the UAV context. The accent on inferring the optimal mission duration without tackling the optimal control formulation head-on constitutes a meaningful advance. This element, which is central to energy efficiency, has received scant dedicated treatment in the extant body of work. Our inquiry fills this void by offering a fresh perspective on the role of mission duration in energy expenditure, yielding important insights for refining UAV operations. The extraction of straightforward rules for reference construction, once the mission time is fixed, introduces a utilitarian element into the study, enabling deployment in real-time settings with reduced computational strain. The paired focus on energy economy and computational practicability augments the hands-on relevance of our contribution within the UAV operations landscape. The concluding stage of our investigation, which entailed benchmarking controller behavior for trajectory regulation using a commercial simulation platform, provided a tangible validation dimension to our study. Appraising energy draw via battery state of charge (SOC) and dissecting the energy-cost functional selected to resolve the optimal control task yielded meaningful insights into the real-world suitability and effectiveness of the proposed controllers. The joint use of a commercial-grade physical drone representation (Simcenter Amesim) alongside a simplified construct for controller synthesis illustrated the adaptability inherent in our methodology. The side-by-side evaluation of these representations enabled a thorough assessment of controller performance across varying levels of system complexity. Such scrutiny is indispensable for gauging the sturdiness and flexibility of the proposed controllers within practical deployments. Our investigation, by weaving together theoretical understanding, optimal control resolutions, and hands-on simulations, adds to a rounded appreciation of energy-efficient trajectory governance for UAVs. It presents a pragmatic architecture that bridges theoretical progress with genuine applicability, making it a worthwhile enrichment to the domain of UAV control systems.

The layout of the paper's remaining segments follows a coherent sequence. A concise outline is given below:

© 2023 The Author(s). | Published by Agro Intelligence Research Press

· Section 2: Presentation of the quadrotor's dynamical representation and the electrical characterization of a brushless DC motor.

· Section 3: Particulars on parameter identification for the selected model, carried out with reference to the commercial physical representation grounded in Simcenter Amesim and supplied by Siemens.

· Section 4: Statement and resolution of the optimal control task employing the identified model, encompassing an examination of optimal control outcomes and the distillation of rules for producing near-optimal mission duration and state-variable setpoints.

· Section 5: Construction and realization of the hierarchical controller.

· Section 6: Evaluation of the hierarchical controller's efficacy, notably regarding trajectory adherence and energy/battery drain.

· Section 7: Inferences extracted from the research outcomes, along with a consideration of prospective future investigative avenues.

This organization provides a clear, logical progression for readers to trace the research approach, findings, and conclusions. It appears to smoothly steer the audience across the successive phases of the endeavor, spanning modeling through to control synthesis and simulation.

Modeling the Energetics of UAV Operations

In this section, we provide a concise overview of the differential and algebraic relationships that govern the UAV's energy behavior. For exhaustive formulas and a deeper understanding, we point readers to the works cited throughout this section, most notably Morbidi *et al.* [27]. These sources provide detailed perspectives on the mathematical foundation supporting the UAV's energy framework, serving as a valuable resource for readers seeking thorough information.

Characterizing Brushless-DC-Motor dynamics in UAVs

This portion addresses the brushless-DC-motor representation, including energy losses in resistive and inductive coil windings and the work required to overcome internal and load-associated friction. The expression for the instantaneous current (t) is worked out from the fundamentals laid down in Gieras [35]. This encompassing treatment establishes a groundwork for grasping the complex energy interplay inside the brushless DC motor, an essential element within the broader energy construct of unmanned aerial vehicles (UAVs):

$$i(t) = \frac{1}{K_T}\left[T_f + T_L(\omega(t)) + D_f\omega(t) + (J_m + J_L)\frac{d\omega(t)}{dt}\right]. \quad (1)$$

In this motor dynamics description, central parameters and variables play key roles. The torque constant of the motor, labeled KT, couples with the angular speed of the motor shaft, (t). In addition, the motor's dynamic behavior incorporates the speed-sensitive load friction torque, $TL(\omega(t))$, originating from propeller drag, the motor's inherent friction torque, Tf, the viscous damping factor of the motor, Df, and the moments of inertia of the motor and load, Jm and JL, in that order. The electric potential across the motor, written as (t), is

© 2023 The Author(s). | Published by Agro Intelligence Research Press

$$e(t) = R\,i(t) + K_E\omega(t) + L\frac{di(t)}{dt}, \quad (2)$$

Where R and L stand for the resistance and inductance of the phase winding, respectively, and KE signifies the voltage constant of the motor. In steady-state operation, the current (t) holds steady, and **Eq. 2** simplifies to

$$e(t) = R\ i(t) + K_E\omega(t), \quad (3)$$

Where (t)=$KE\omega$(t) denotes the counter-electromotive force of the motor (the voltage that resists the current variation producing it), within our electrical framework, several idealizations have been adopted to keep the analysis tractable. The influence of the electronic speed controller (ESC) positioned between the LiPo battery and the brushless motor, alongside the energy dissipated within the battery owing to non-idealities, is disregarded (see **Figure 1** in Morbidi *et al.* [27]). Likewise, it is presumed that the motor shaft couples straight to the propeller without any gearbox intervening. These idealizations, commonly applicable to off-the-shelf quadrotors such as the DJI Phantom 2/3, AscTec Pelican, and Parrot Bebop, aid in forming a lean model for interpreting and evaluating the UAV's energy characteristics.

Quadrotor dynamic model

We begin by letting the vector (x,,) ^{T} locate the quadrotor's center of mass within the stationary inertial frame $\mathcal{E}$. Turning to angular motion, the triplet (ϕ,,) ^{T} captures the rotational orientation: ϕ tracks roll about the x-axis, θ captures pitch about the y-axis, and ψ measures yaw about the z-axis. Affixed to the quadrotor's stiff cross-type airframe are a set of four matching brushless DC motors. The counterclockwise-spinning pair consists of motors 1 and 3, while motors 2 and 4 turn clockwise—both directions defined relative to the body frame's z-axis ($\mathcal{B}$). Each motor runs at an angular velocity $\omega j \geq 0$ and, in undisturbed air, produces a thrust force fj, where $j \in 1,2,3,4$. An exhaustive dynamical account of the quadrotor, complete with the full motion equations [27, 36-39].

When attitude angles stay small, the quadrotor's motion can be captured by the following compact system:

$$\begin{aligned} m\ddot{x} &= (\sin\phi\ \sin\psi + \cos\phi\ \cos\psi\ \sin\theta)\ u_z \\ m\ddot{y} &= (\cos\phi\ \sin\theta\ \sin\psi - \cos\psi\ \sin\phi)\ u_z \\ m\ddot{z} &= (\cos\theta\ \cos\phi)\ u_z - mg \\ \ddot{\phi} &= u_\phi, \quad \ddot{\theta} = u_\theta, \quad \ddot{\psi} = u_\psi, \end{aligned} \quad (4)$$

In this representation, the synthetic input terms—namely uz (force exerted along the body-frame z-direction), together with $u\phi$, $u\theta$, and $u\psi$ (the respective torques acting around the x, y, and z axes)—are expressed as instantaneous functions of the velocity states, position coordinates, and motor states of the UAV:

© 2023 The Author(s). | Published by Agro Intelligence Research Press

$$\begin{aligned} u_z &= \kappa_b\left(\omega_1^2+\omega_2^2+\omega_3^2+\omega_4^2\right) \\ u_\phi &= \frac{I_y-I_z}{I_x}\dot{\theta}\dot{\psi}+\frac{l}{I_x}\kappa_b\left(\omega_2^2-\omega_4^2\right)-\frac{J}{I_x}\dot{\theta}\left(\omega_1-\omega_2+\omega_3-\omega_4\right) \\ u_\theta &= \frac{I_z-I_x}{I_x}\dot{\phi}\dot{\psi}+\frac{\ell}{I_x}\kappa_b\left(\omega_3^2-\omega_1^2\right)+\frac{J}{I_x}\dot{\phi}\left(\omega_1-\omega_2+\omega_3-\omega_4\right) \\ u_\psi &= \frac{I_x-I_y}{I_z}\dot{\phi}\dot{\theta}+\kappa_\tau\frac{\left(\omega_1^2+\omega_3^2-\omega_2^2-\omega_4^2\right)}{I_z}. \end{aligned} \quad (5)$$

The foregoing expressions collectively define the reduced dynamic model of the quadrotor. Their constituent symbols are defined as follows:

g is the constant of gravitational acceleration;

m corresponds to the total vehicle mass;

J equals the net inertia contributed by one motor;

I=diag(Ix,Iy,Iz) is the diagonal matrix encoding the rotorcraft's rotational inertias;

κb and $\kappa\tau$ label the propeller thrust factor and aerodynamic drag factor, respectively [40];

ℓ measures the span between an individual motor and the vehicle's center of mass.

Altogether, these relations approximate the quadrotor's dynamic response, incorporating the downward pull of gravity, the upward thrust delivered by the spinning propellers, and the resistive influence of aerodynamic drag torque.

In accordance with Li and Peng [40]:

$$\kappa_b = C_T\rho A r^2, \kappa_\tau = C_Q\rho A r^3, \quad (6)$$

In the above, mB refers to the mass of a single blade, nB indicates how many blades constitute the propeller, ϱ is ambient air density, ϵ specifies the radial offset separating the blade root from the motor hub, r and A=πr2 give the propeller's radius and swept disk area, respectively, CT stands for the propeller's dimensionless thrust coefficient (a quantity shaped by the propeller's geometric profile), $\frac{CQ}{=CT\sqrt{CT/2}}$ and denotes the companion torque coefficient.

Energy and motor efficiency

The total energy expended by the quadrotor across a predetermined mission window can be quantified through the relation:

$$E = \int_{t_0}^{t_f}\sum_{j=1}^{4} e_j(t)\ i_j(t)\ dt. \quad (7)$$

© 2023 The Author(s). | Published by Agro Intelligence Research Press

As elaborated more fully by Morbidi *et al.* [27]—which interested readers should consult for expanded derivations—this formula integrates instantaneous electrical power (the voltage–current product) over the time horizon of interest. The integer subscripts 1, 2, 3, and 4 index each of the four onboard motors. Carrying out the integration yields a scalar measure of the cumulative energy drawn by the propulsion system throughout that interval. Should we incorporate the governing electrical-motor dynamics and further impose the condition that $\omega(t0)=\omega j(tf)$ holds for every $j\in1,2,3,4$—which enforces identical starting and ending angular velocities on all motors (a requirement that enters the optimal-control formulation as an explicit constraint [40])—then the energy integral admits a far tidier equivalent:

$$E = \int_{t_0}^{t_f} \sum_{f=1}^{4} \left(c_1 + c_2\omega_f(t) + c_3\omega_f^2(t) + c_4\omega_f^3(t) + c_5\omega_f^4(t) + c_6\dot{\omega}_f^2(t) \right) dt, \quad (8)$$

Within this condensed form, $\dot{\omega}(t)$ denotes the angular acceleration experienced by the j-th motor, while the scalars $c1,\cdots,c6$ are constants whose values follow directly from the motor parameters and propeller geometry. Moving to the battery's state-of-charge computation, for any instant within the interval $t\in[t0,tf]$ define

$$i_{\text{dis}}(t) = \left(\sum_{k=1}^{4} \left(T_f + \kappa_\tau \omega_k^2(t) + D_f \omega_k(t) \right) + J \sum_{f=1}^{4} \alpha_f(t) \right) / K_T \quad (9)$$

As the instantaneous discharge current supplied by the quadrotor's battery when flying the minimum–energy path. Once the discharge-current profile $i\text{dis}(t)$ is known over $t\in[t0,tf]$, the corresponding SOC trajectory can be reconstructed using the well-known "two-well" kinetic battery model (KiBaM, summarized here; a thorough treatment is offered by Jongerden and Haverkort [41]):

$$\begin{aligned} \dot{y}_1(t) &= -i_{\text{dis}}(t) + k_f\left(h_2(t) - h_1(t)\right) \\ \dot{y}_2(t) &= -k_f\left(h_2(t) - h_1(t)\right). \end{aligned} \quad (10)$$

The system of equations just presented models how charge redistributes in an idealized two-reservoir battery: reservoir one holds the available charge ($y1$), while reservoir two stores the bound charge ($y2$). The coefficient kf sets the characteristic rate at which charge migrates from the bound well into the available well. Initial values for both reservoirs are fixed at the start time $t0$. The parameter C denotes the battery's nameplate capacity, and γ specifies what share of that total capacity initially populates the available-charge reservoir. Conceptually, the model tracks the internal movement of charge between these coupled reservoirs under the influence of the discharge current. The available well receives an initial allocation of γC, leaving the bound well with the complementary portion $(1-\gamma)$C. The inter-well transfer rate is modulated by kf. Complete exhaustion—a fully discharged state—is reached precisely when the available charge well empties entirely, i.e., when $y1=0$.

Parameter Identification of Quadrotor Model

Turning now to the numerical values that populate the quadrotor model, the mechanical parameters appearing in **Eqs. 4, 5** are firmly established: m=5 kg; g=9.81 m · s^{-2}; l=0.3 m; Ix=0.011521 kg · m^2; Iy=0.0362132 kg · m^2; Iz=0.029142 kg · m^2; J=0.0003 kg · m^2; κb=4.5625·10^{-5} N · s^2· rad−2; $\kappa\tau$=1.375·10^{-5} N · s^2· rad^{-2}· m. The electrical sub-model and the precise motor geometry, however, are not known to the same degree of certainty; as a consequence, the six coefficients ci, i=1,…,6 appearing in energy functional (8) remain undetermined. To resolve this uncertainty, we employ least-square

© 2023 The Author(s). | Published by Agro Intelligence Research Press

estimation (LSE), minimizing the discrepancy between the four-motor energy trajectories generated by Simcenter Amesim—Siemens' high-fidelity commercial physical modeling environment (a detailed description of this tool is deferred to Section 6.2)—and those predicted by our parametric model. Formally, we minimize:

$$E_{AME,j}(t) = \int_{t_0}^{t} e_{AME,j}(\tau)\ i_{AME,j}(\tau)\ d\tau, \quad (11)$$

Here $eAME,(t)$ and $iAME,j(t)$, with $j\in1,2,3,4$, represent the per-motor voltages and currents extracted from the Amesim quadrotor simulation, and the companion modeled energy trajectories, derived from **Eqs. 4-5**, are expressed as

$$E_j(t) = \int_{t_0}^{t} \left(c_1 + c_2\omega_j(\tau) + c_3\omega_j^2(\tau) + c_4\omega_j^3(\tau) + c_5\omega_j^4(\tau) + c_6\dot{\omega}_j^2(\tau)\right) d\tau, \quad (12)$$

Both correspond to the same flight maneuver (hence, identical inputs), with the transformation exploiting the demonstrated equality between the integral formulation (7) and the parametric form (8). The parameter-fitting calculation was performed inside MATLAB by invoking the lsqnonlin routine, which carries out ordinary least-square minimization over the residual sequence $EAME-E$. In this procedure, $EAME$ and E denote vectors that collect uniformly sampled values (sampling step fixed at 0.01 s) of the functions defined in (11) and (12), respectively, concatenated across all four motors and over the entire maneuver timeline. The optimization converged to the following best-fit parameter estimates for the energy functional (8): $\hat{c}1=2 = 2.3324$, $\hat{c}2 = 0.0420$, $\hat{c}3 = 1.7274 \cdot10-4$, $\hat{c}4 = 1.4534 \cdot10-8$, $\hat{c}5 = 1.2520 \cdot10-9$, $\hat{c}6 = 7.3230 \cdot10-4$. Shifting attention to the KiBaM battery representation in (10), the kinetic parameters kf and γ were adopted directly from the values reported by Morbidi *et al.* [27], while the (known) total capacity of the Simcenter Amesim battery pack was taken as C=9.06136 Ah. Setting the initial state of charge to 95% of the rated capacity (so that $y1(0)+y2(0)=0.95C$), **Figure 1** confirms a near-perfect match between the discharge curve predicted by the Amesim environment and the curve produced by the quadrotor model after recalibrating the dynamical parameters from Morbidi *et al.* [27] with the updated total capacity value. The chosen battery technology is LiPo, characterized by a nominal terminal voltage of 22 V and a discharge rating of 25 C. Its model was parameterized via the battery pre-sizing module within Simcenter Amesim. This module constructs lookup tables describing how the open-circuit voltage, entropic coefficient, and discharge resistance vary as functions of both state of charge and cell temperature. Construction of these tables draws on a trio of target specifications—terminal voltage, energy capacity, and power capability—combined with an extensive built-in database spanning a wide range of synthesized battery chemistries.

© 2023 The Author(s). | Published by Agro Intelligence Research Press

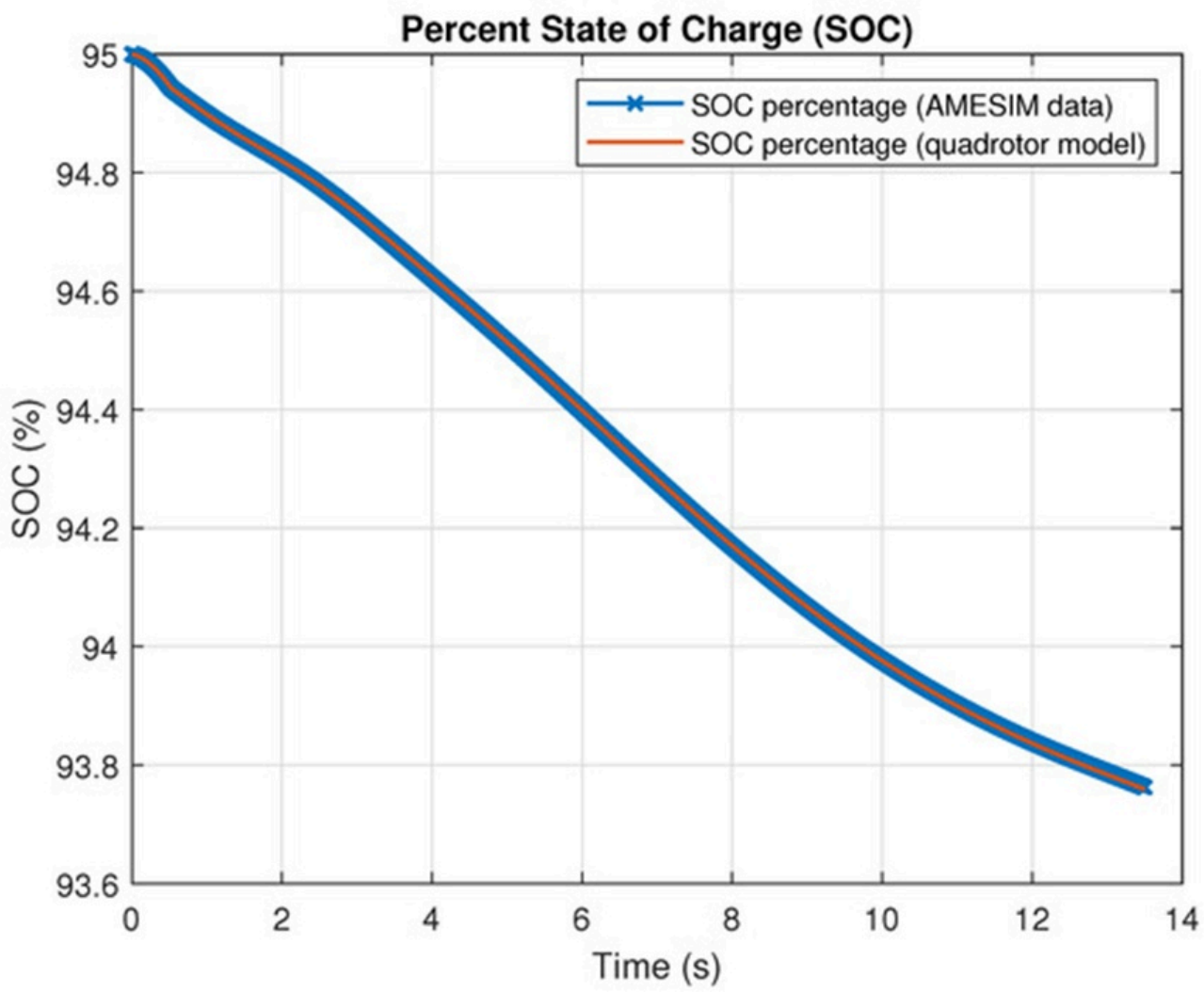

Figure 1. Electrical model of the brushless DC motor of a quadrotor UAV.

Energetic Rule–Based Reference Generation Based on Optimal Control

This section formulates and solves an optimal-control (OC) problem that transitions the quadrotor from a given start state to a designated end state, with the overarching objective of minimizing energy consumption. A detailed post-solution examination of the OC results is then undertaken, distilling practically useful rules for pinpointing both the energetically optimal mission duration and the associated reference-generation logic. These derived outputs serve as indispensable ingredients for the later incorporation of closed-loop control into UAV missions.

Optimal control problem

This stage entails recasting the system description into state-space format by defining a suitable state vector. Such a reformulation is deliberately pursued to compress the system representation, paving the way for sharper analysis and more streamlined control design: $\mathbf{x}=(x1,\cdots,xn)T\in\mathbb{R}n$, where n=16, and the input vector $\alpha=(\alpha1,\alpha2,\alpha3,\alpha4)$ $T\in\mathbb{R}p$, with p=4. The individual assignments are made as follows: $x1=x,x2=\dot{x}$ $1,x3=y,x4=\dot{x}$ $3,x5=z,x6=\dot{x}$ 5 $x7=\phi,x8=\dot{x}$ $7,x9=\theta,x10=\dot{x}$ $9,x11=\psi,x12=\dot{x}$ 11 $x13=\omega1,\dot{x}$ $13=\alpha1,x14=\omega2,\dot{x}$ $14=\alpha2$ $x15=\omega3,\dot{x}$ $15=\alpha3,x16=\omega4,\dot{x}$ $16=\alpha4$. Following this augmentation, the quadrotor model takes the upgraded form [27].

© 2023 The Author(s). | Published by Agro Intelligence Research Press

$$
\begin{aligned}
\dot{x}_1 &= x_2, \\
\dot{x}_2 &= \frac{\kappa_B}{m}(\sin x_7 \sin x_{11} + \cos x_7 \cos x_{11} \sin x_9) \sum_{k=13}^{16} x_k^2, \\
\dot{x}_3 &= x_4, \\
\dot{x}_4 &= \frac{\kappa_B}{m}(\cos x_7 \sin x_9 \sin x_{11} - \cos x_{11} \sin x_7) \sum_{k=13}^{16} x_k^2, \\
\dot{x}_5 &= x_6, \\
\dot{x}_6 &= \frac{\kappa_B}{m}(\cos x_9 \cos x_7) \sum_{k=13}^{16} x_k^2 - g \\
\dot{x}_7 &= x_8, \\
\dot{x}_8 &= (\frac{I_y - I_z}{I_x}) x_{10} x_{12} + \frac{\ell \kappa_B}{I_x}(x_{14}^2 - x_{16}^2) - \frac{J}{I_x} x_{10}(x_{13} + \\
&\quad -x_{14} + x_{15} - x_{16}), \\
\dot{x}_9 &= x_{10}, \\
\dot{x}_{10} &= (\frac{I_z - I_x}{I_y}) x_8 x_{12} + \frac{\ell \kappa_B}{I_y}(x_{15}^2 - x_{13}^2) + \frac{J}{I_y} x_8(x_{13} - \\
&\quad +x_{14} + x_{15} - x_{16}), \\
\dot{x}_{11} &= x_{12}, \\
\dot{x}_{12} &= (\frac{I_x - I_y}{I_z}) x_8 x_{10} + \frac{\kappa_T}{I_z}(x_{13}^2 - x_{14}^2 + x_{15}^2 - x_{16}^2), \\
\dot{x}_{13} &= \alpha_1, \dot{x}_{14} = \alpha_2, \dot{x}_{15} = \alpha_3, \dot{x}_{16} = \alpha_4,
\end{aligned}
\tag{13}
$$

Which admits a tidy restatement in input–affine fashion:

$$\dot{\mathbf{x}}(t) = f(\mathbf{x}(t)) + B\alpha(t), \tag{14}$$

With the function $f{:}\mathbb{R}^{16} \to \mathbb{R}^{16}$ bundling every state-driven contribution appearing in the transformed system (13), and $B = \begin{pmatrix} 012 \times 12 & 012 \times 4 \\ 04 \times 12 & I4 \times 4 \end{pmatrix}$, where the symbols $\mathbf{0}$ and I respectively denote zero blocks and identity blocks of matching dimensions. Once the energy-based performance measure (7) and the dynamics (14) are both available, the optimal control problem can be formally introduced as:

$$\min_{\alpha} E = \int_{t_0}^{t_f} \left(\sum_{k=13}^{16} \left(c_1 + c_2 x_k(t) + c_3 x_k^2(t) + c_4 x_k^3(t) + c_5 x_k^4(t) \right) + c_7 \sum_{f=1}^{4} \alpha_f^2(t) \right) dt, \tag{15}$$

© 2023 The Author(s). | Published by Agro Intelligence Research Press

Under the constraint ($t0$) = $xt0$ = (tf) = xtf. To ensure the motor angular velocities respect pre-imposed technological bounds (0 ≤ xi ≤ ωmax for i = 13, 14, 15, 16), the terminal instant tf is chosen accordingly. Resorting to the Pontryagin minimum principle (PMP) enables the identification of the optimal path and the optimal (open-loop) command history through the running cost L and the Hamiltonian function H expressed as

$$L\left(x\left(t\right),\alpha\left(t\right)\right)=\sum_{k=13}^{16}\left(c_1+c_2x_k\left(t\right)+c_3x_k^2\left(t\right)+c_4x_k^3\left(t\right)+c_5x_k^4\left(t\right)\right)+c_7\sum_{f=1}^{4}\alpha_f^2\left(t\right)$$

(16)

$$H\left(x\left(t\right),\alpha\left(t\right),\lambda\left(t\right)\right)=\lambda^T\left(t\right)\left(f\left(x\left(t\right)\right)+B\alpha\left(t\right)\right)+L\left(x\left(t\right),\alpha\left(t\right)\right),\quad(17)$$

Augmented by the backward costate dynamics fulfilled by the adjoint vector (t)∈$\mathbb{R}n$:

$$-\dot{\lambda}\left(t\right)=\lambda^T\left(t\right)f_x\left(x^\star\left(t\right)\right)+L_x\left(x^\star\left(t\right),\alpha^\star\left(t\right)\right).\quad(18)$$

This relation is directly connected to the boundary-value problem (BVP) that naturally arises in optimal-control frameworks. The terms carry the following meaning:

· tf: Final time of the operation;

· (tf)=**0**: The adjoint vector λ vanishes at the terminal instant. In optimal-control parlance, the costate quantifies how sensitive the cost functional is to infinitesimal perturbations in the state trajectory;

· x★: Optimal state evolution;

· α★: Optimal input function;

· fx and Lx: Jacobian matrices of the mappings f and L, computed with respect to the state vector x.

Taken in combination, **Eqs. 14, 18** jointly define a 2n-dimensional boundary value problem posed on the augmented state (x,). This BVP comes equipped with n initial stipulations and n terminal stipulations acting on the state x. Solving a BVP of this nature is a well-trodden path in optimal control theory for recovering the optimal trajectories and control actions that minimize a prescribed cost integral over a fixed temporal horizon.

Rule–based energetic reference generation

Although controllers or reference-generation blocks that rely on empirical rules are computationally efficient on embedded CPUs, they may deviate significantly from true optimality and can be difficult to tune properly. On the other hand, the optimal solutions produced by the OC problem—one for each mission configuration embedded in the control formulation—yield trajectory datasets ripe for interpretation. By carefully inspecting these optimal trajectories, compact rules that mimic optimal behavior can be teased out. Unlike raw OC profiles, these extracted rules are practically implementable. The first step is to run a large ensemble of simulations across widely varying mission scenarios, thereby building a library of optimal paths and corresponding control strategies. A subsequent pattern-recognition phase then isolates recurring

© 2023 The Author(s). | Published by Agro Intelligence Research Press

structural features in optimal decisions and codifies them into concrete rules. To build a maximally informative dataset, all feasible pairings of initial and terminal states spanning the three translational coordinates are systematically enumerated. The central thrust is to identify an optimal energy-trajectory, with the ambition of furnishing a general-purpose reference suitable for a variety of feedback controllers. The paragraphs below describe how the rules are extracted from this exhaustive numerical campaign.

Optimal mission-time setting

Given a mission framed by the initial and final position coordinates ($x0$,0,$z0$) and (xf,yf,zf), the Euclidean span d is worked out as $d = \sqrt{(xf - x0)^2 + (yf - y0)^2 + (zf - z0)^2}$. This scalar length functions as a decisive quantity that molds the optimal travel time $t$opt, a parameter deeply intertwined with the overall energy draw. How $t$opt varies with d is captured visually in **Figure 2**, which exposes the coupling between the geometric extent and the UAV's intrinsic physical limits, including the maximum permissible motor rotation speed. The concrete parameter set adopted for the UAV under study is deferred to Section 6. Alterations to the UAV specifications result in a shift of the linear fit, visualized as a positive offset (orange straight line) or a negative offset (green straight line) in **Figure 2**. Which direction the line moves hinges on whether the airframe is swapped for a less capable or a more capable platform. A recommended practice is to increase the line's intercept in small steps while maintaining an operating margin to avoid actuator saturation. This measured approach helps secure optimal behavior while remaining within the UAV's design envelope.

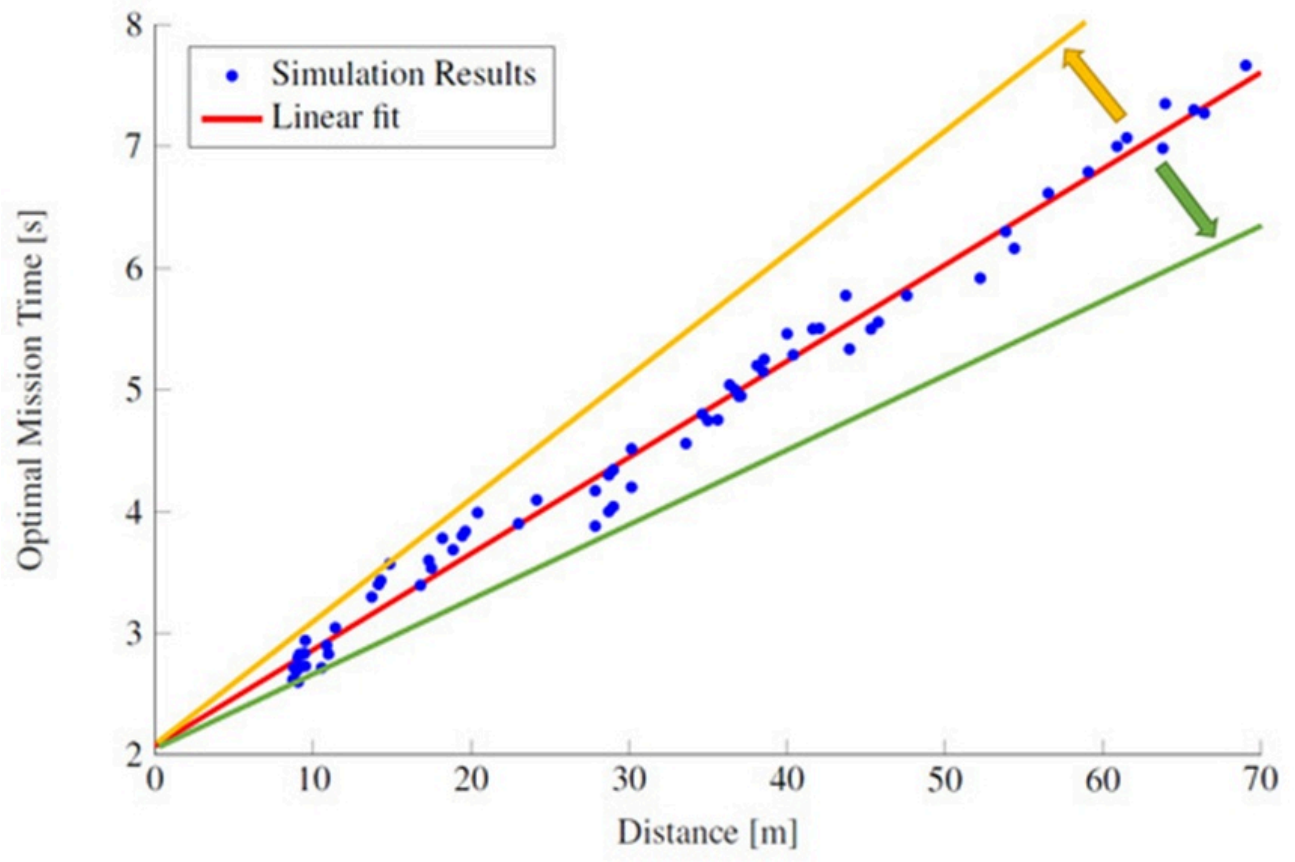

Figure 2. Battery-state-of-charge (SOC) trajectory in Simcenter Amesim and in the simplified quadrotor model.

Optimal trajectory references

With $t$opt fixed, the solution of the optimal control problem described in Section 4.1 is dissected to yield sub-optimal position and velocity profiles along each of the three reference axes. **Figure 3** plots the optimal position and velocity

© 2023 The Author(s). | Published by Agro Intelligence Research Press

patterns for four missions picked at random from a broad spectrum of simulated scenarios. The left column traces the time histories of $x$opt, $y$opt, and $z$opt, while the right column gives the corresponding velocity traces $\dot{x}$opt, $\dot{y}$opt, and $\dot{z}$opt. For full generality, every mission is launched from the coordinate origin, with the target endpoints set to: [6,6,3], [8,6,10], [17,8,5], [10,10,10]. Each mission has a unique optimal duration, a quantity closely governed by the separation length and captured by the regression line in Section 4.2.1. Across the tested missions, parabolic curves provide faithful approximations of the optimal reference velocity evolutions, with the parabola attributes being influenced by the optimal mission duration ($t$opt), the path length (d), and the terminal coordinate values. Thanks to this observation, near-optimal energetic velocity reference signals for all three axes can be synthesized without any need to tackle the optimal control problem repeatedly. The parabolic forms prescribed for the optimal-energetic-velocity profiles on each axis read:

$$k_{\text{ref}}(t) = at^2 + bt + c, \quad t \in [0, t_{\text{opt}}]. \tag{19}$$

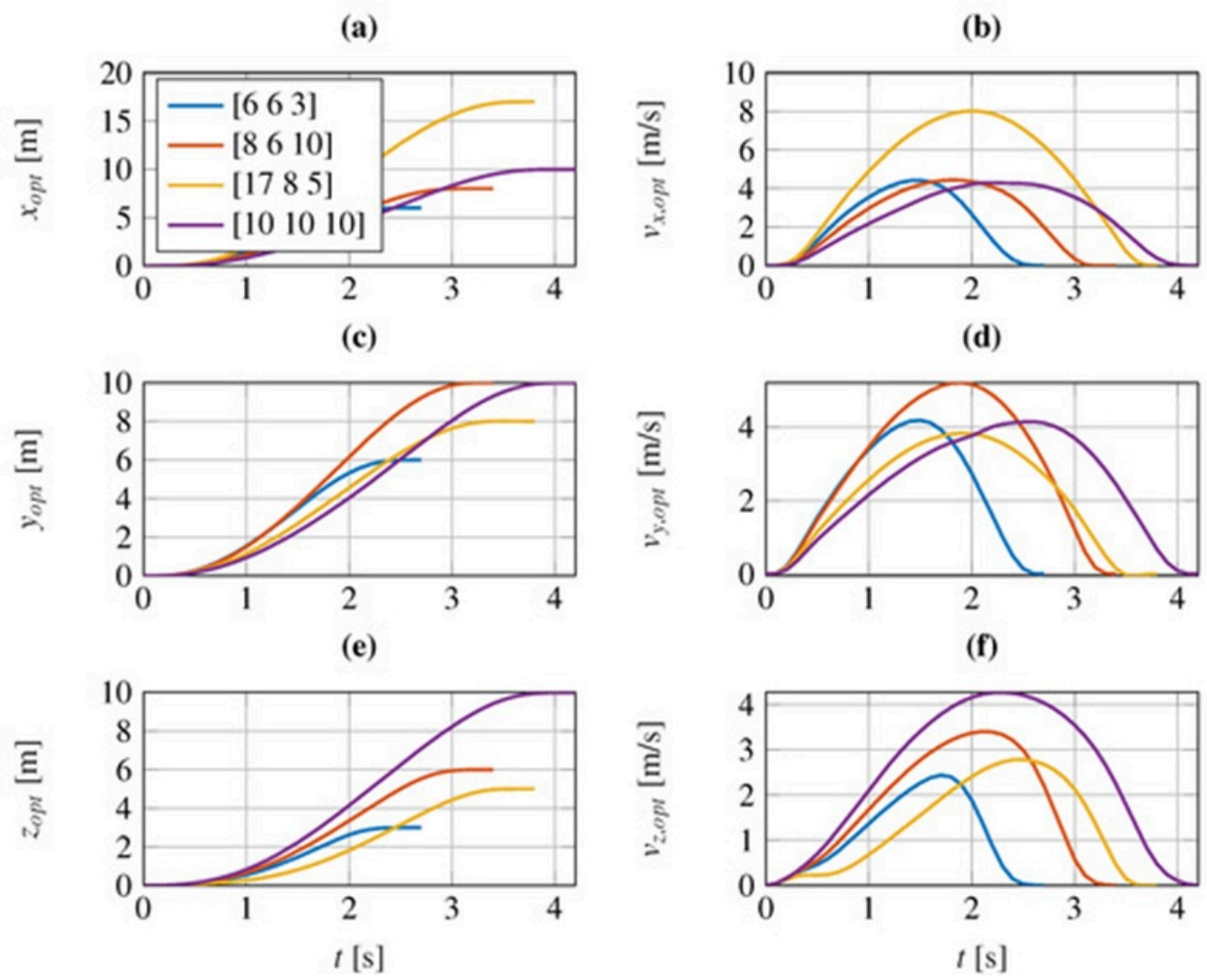

Figure 3. Dependence of the optimal mission time on distance d. The blue markers correspond to optimal times as functions of distance, extracted from solutions to the optimal control problem. At the same time, the red trace is a linear approximation fitted to those data points. The orange and green straight lines illustrate how the linear fit shifts up or down as UAV characteristics are modified.

© 2023 The Author(s). | Published by Agro Intelligence Research Press

In these expressions, the trio of coefficients a, b, c together with the shaping factor KM set the parabola's curvature; k0 denotes the starting value, and $k$ref represents the reference velocity belonging to whichever axis is under consideration. The shaping factor kM, which controls the peak height of the parabola, is calculated from the axis's final value kf together with $k$opt(d), a generator-tuning term that exhibits dependence on d:

$$k_M = k_{\text{opt}}(d)\ k_f. \quad (20)$$

Once the parabolic surrogates for the optimal velocity references on all three axes have been fixed, the next logical move is to integrate them to reconstruct the positional reference trajectories. The integration step ensures a smooth, mutually consistent representation of the UAV's optimal route. Enforcing the initial specification γref(0)=γ0 where γref∈{$x$ref,$y$ref,$z$ref}, one arrives at

$$\gamma_{\text{ref}}(t) = \frac{a}{3}t^3 + \frac{b}{2}t^2 - k_0 t + \gamma_{\text{ref}}(0), \quad (21)$$

This stands as the approximate optimal position trajectory. A scrutiny of the structural regularities displayed by the optimal position references suggests that cubic polynomials are well matched to the task of approximating these time functions. In parallel, the optimal energetic yaw-rate trajectory and its rate of change can be determined and approximated, respectively, by a cubic polynomial and a parabolic profile. Summing up, the generation of near-optimal energetic reference trajectories becomes completely feasible without once invoking an optimal control solver, thereby furnishing instantaneous setpoints for tracking positions, yaw rate, and their first derivatives.

Hierarchical Real–Time Control

As a reminder, the (open-loop) optimal control solution presented in Section 4.1 is generated in advance. It serves a twofold purpose: synthesizing energetic reference trajectories and providing a benchmark for evaluating controller behavior. What is actually fielded for UAV guidance is a nonlinear feedback-control methodology rooted in the classical hierarchical scheme detailed in Carrillo *et al.* [37]. Deploying this methodology secures genuine real-time flexibility and reactivity when directing the UAV along its designated route. Execution of the controller occurs in discrete time: the virtual control actions uz, $u\phi$, $u\theta$, $u\psi$ from (4) are kept unchanged throughout each sampling window [ti,+1), with the step duration satisfying ti+1−ti=Δt for i=0,⋯,$i$max−1 and timax=tf. Operating in this sampled-data mode preserves stability and enables tight regulation within each interval, thereby reinforcing the overall performance of the UAV control system. To make the synthesis more manageable, the motor dynamics ωi, i=1,2,3,4 are deliberately disregarded during the early design phase. They are brought back only in the final stage via digital approximation, together with **Eq. 5**. The initial design effort is concentrated on dictating the target closed-loop response for the vertical position–velocity pair. Restricting attention to this subsystem simplifies the handling of specific control objectives before the extra layer of motor transients is introduced:

$$\ddot{z}(t) = \ddot{z}_{\text{ref}}(t) - k_{pz}(z(t) - z_{\text{ref}}(t)) - k_{dz}(\dot{z}(t) - \dot{z}_{\text{ref}}(t)), \quad (22)$$

Where the gains are positive (kpz,z>0), the reference signals are sourced from the optimal plan as $z$ref(t)=x★5(t), $z\dot{}$ ref(t)=x★6(t), with x★ denoting the precomputed optimal trajectory (see Section 4.1), and $z\ddot{}$ref(t) can be evaluated through numerical differentiation. **Eq. 22** with the third relation in (4) produces the linearizing control expression,

© 2023 The Author(s). | Published by Agro Intelligence Research Press

$$u_z(t) = m\frac{\ddot{z}_{\text{ref}}(t) - k_{pz}e_z(t) - k_{dz}\dot{e}_z(t) + g}{\cos\theta\ \cos\phi}, \quad (23)$$

Once the vertical mismatch is defined as $(t)=z(t)-z\text{ref}(t)$. Picking a linearizing regulator that operates on the vertical position–velocity pair $(z,\dot{})$ through the gains kpz and kdz has the effect of collapsing this pair into a pure integrator chain. Thanks to the gains kpz and kdz, the corresponding error dynamics become exponentially stable. Mirroring the same line of reasoning, the linearizing controller is also deployed to enforce the intended closed-loop response for the yaw angle and its derivative. This methodical construction locks in stability and imposes the required dynamics on the controlled quantities:

$$u_\psi(t) = \ddot{\psi}(t) = \ddot{\psi}_{\text{ref}}(t) - k_{p\psi}e_\psi(t) - k_{d\psi}\dot{e}_\psi(t), \quad (24)$$

With positive gains $kp\psi,kd\psi>0$, after introducing the yaw tracking error $e\psi(t)=\psi(t)-\psi\text{ref}(t)$ and adopting the reference mappings $\psi\text{ref}(t)=x\bigstar 11(t)$, $\psi\dot{}\,\text{ref}(t)=x\bigstar 12(t)$. Substituting (23) back into (4) and dropping the time arguments for brevity yields:

$$\begin{aligned}\ddot{x} &= \left(\frac{\tan\phi\sin\psi}{\cos\theta} + \cos\psi\tan\theta\right)\left(\ddot{z}_{\text{ref}} - k_{pz}e_z - k_{dz}\dot{e}_z + g\right)\\ \ddot{y} &= \left(\tan\theta\sin\psi - \frac{\cos\psi\tan\phi}{\cos\theta}\right)\left(\ddot{z}_{\text{ref}} - k_{pz}e_z - k_{dz}\dot{e}_z + g\right).\end{aligned} \quad (25)$$

The core idea of the hierarchical-control strategy is the use of large gain values kpz, kdz, $kp\psi$, $kd\psi$ to induce rapid vertical and yaw transients. When these gains are set sufficiently high, the position and velocity discrepancies in the yaw and vertical channels shrink to near-zero levels well before the end of each sampling slot $[ti,ti+1)$. This behavior justifies a convenient reduced-order simplification wherein those discrepancies are treated as effectively zero throughout each interval, substantially lightening the control computations:

$$\ddot{x} = \left(\frac{\tan\phi\sin\psi}{\cos\theta} + \cos\psi\tan\theta\right)\left(\ddot{z}_{\text{ref}} + g\right) \quad (26)$$

$$\ddot{y} = \left(\tan\theta\sin\psi - \frac{\cos\psi\tan\phi}{\cos\theta}\right)\left(\ddot{z}_{\text{ref}} + g\right). \quad (27)$$

The desired closed-loop response for the horizontal $(x,)$ position–velocity pairs is formulated as

$$\ddot{x}(t) = \ddot{x}_{\text{ref}}(t) - k_{px}e_x(t) - k_{dx}\dot{e}_x(t) \quad (28)$$

© 2023 The Author(s). | Published by Agro Intelligence Research Press

$$\ddot{y}(t) = \ddot{y}_{\text{ref}}(t) - k_{py}e_y(t) - k_{dy}\dot{e}_y(t), \quad (29)$$

With positive gains $kpx,kdx,kpy,kdy>0$ and the error quantities $ex(t)=x(t)-x\text{ref}(t)$, $ey(t)=y(t)-y\text{ref}(t)$, the reference signals being extracted from the optimal trajectory as $x\text{ref}(t)=x\bigstar1(t)$, $\dot{x}\,\text{ref}(t)=x\bigstar2(t)$, $y\text{ref}(t)=x\bigstar3(t)$, $\dot{y}\,\text{ref}(t)=x\bigstar4(t)$. Placing (26) and (27) alongside (28) and (29), and exploiting the small-angle approximation $\cos\theta\approx1$ in the denominator of (26), delivers closed-form approximate expressions for the attitude reference angles (ϕ,). These expressions directly enforce the dynamics mandated by (28) and (29). Such an analytical pathway sharpens the understanding and streamlines the practical implementation of the target UAV control behavior:

$$\phi_{\text{ref}} = \arctan\left(\sin\theta\tan\psi - \frac{\cos\theta\left(\ddot{y}_{\text{ref}} - k_{py}e_y - k_{dy}\dot{e}_y\right)}{\left(\ddot{z}_{\text{ref}} + g\right)\cos\psi}\right) \quad (30)$$

$$\theta_{\text{ref}} = \arctan\left(\frac{\ddot{x}_{\text{ref}} - k_{px}e_x - k_{dx}\dot{e}_x}{\left(\ddot{z}_{\text{ref}} + g\right)\cos\psi} - \tan\phi\tan\psi\right) \quad (31)$$

To compel the (ϕ,θ) dynamics to track the reference values (ϕref, ref) with minimal lag, extra constraints are imposed. These additional stipulations enhance the overall steadiness and precision of the control framework, guaranteeing that the UAV swiftly settles onto the commanded orientation:

$$u_\phi(t) = \ddot{\phi}(t) = -k_{p\phi}\left(\phi(t) - \phi_{\text{ref}}\right) - k_{d\phi}\dot{\phi}(t) \quad (32)$$

$$u_\theta(t) = \ddot{\theta}(t) = -k_{p\theta}\left(\theta(t) - \theta_{\text{ref}}\right) - k_{d\theta}\dot{\theta}(t), \quad (33)$$

Where the gain parameters are chosen amply large, i.e., $kp\phi,kd\phi,kp\theta,kd\theta>0$, as noted at the outset of this section, a digital realization of the control laws uz, $u\psi$, $u\phi$, $u\theta$ specified in (22), (23), (32) and (33) is achieved by sampling the right-hand sides of those formulas at each instant ti and then holding the resulting values $uz(ti)$, $u\psi(ti)$, $u\phi(ti)$, $u\theta(ti)$ constant throughout the interval $[ti,ti+1)$. The final operation involves translating these into the physical actuation commands (ti), $j=1,2,3,4$—namely, the four motor angular accelerations—that feed **Eq. 14**. Toward this end, the measured angular rates $\phi(ti)$, $\theta(ti)$, $\psi(ti)$ and the virtual input values $uz(ti)$, $u\psi(ti)$, $u\phi(ti)$, $u\theta(ti)$ are combined to partially invert (5) and recover the demanded motor speeds $\omega j(ti)$, $j=1,2,3,4$. The digital actuation samples are then formed, via a first-order discretization applied to the final equations in (14), as

$$\alpha_j(t_l) = \frac{\omega_j(t_l) - \omega_j(t_{l-1})}{\Delta t} \qquad j = 1,2,3,4. \quad (34)$$

Simulation Results

This segment evaluates the performance of the proposed control solution. A description of the simulation infrastructure is provided first, followed by the outcomes recorded when the controller operates on the Simcenter Amesim Drone model.

© 2023 The Author(s). | Published by Agro Intelligence Research Press

The section concludes with closing reflections centered on energetic considerations, furnishing a thorough appraisal of the controller's merits and its influence on UAV dynamic response.

Co-simulation environment with Matlab and Simcenter Amesim

The impetus for bringing numerical simulation into the present investigation stems from its ability to probe controller behavior when connected to a plant representation or a virtual mock-up of the UAV. System-level simulation is especially well-suited to this end, as it allows the assembly of a dynamic, multi-physics performance model of the UAV whose fidelity is sufficient to robustly assist the iterative maturation of sophisticated control algorithms, including their virtual verification and validation (V&V) [42]. The software platforms selected for this inquiry were MATLAB/Simulink, used to model and simulate the controllers, and Simcenter Amesim, which served as the dynamic, multi-physics simulation environment [43]. Produced by Siemens Digital Industries Software, Simcenter Amesim provides access to pre-built components in libraries covering multiple physical (fluids, mechanical, electrical, thermal) and application-focused (aerospace, automotive, gas turbines) areas. These elements are naturally suited to represent the various UAV subsystems, including energy storage (e.g., lithium-ion batteries), propulsion (e.g., electric motors and propellers), and flight mechanics. As discussed by Cappuzzo *et al.* [42], UAV subsystem models constructed with this tool have been favorably matched against experimental data released by manufacturers or documented in the academic literature. The co-simulation strategy capitalizes on the complementary strengths of the two chosen tools, enabling exploration of controller response across a wide range of operating scenarios expected throughout a UAV mission, including off-nominal and fault conditions.

Compared to the reference mathematical model that guided the controller design in Section 2, the Simcenter Amesim plant model offers significantly greater richness, incorporating additional physical effects and parameters that drift over time. As a result, it also serves as a credible test bench for the controller. A direct consequence is that the parameters embedded inside the model-based controller required identification, a procedure undertaken in Section 3. For example, the aerodynamic properties of the propellers—specifically the thrust and drag coefficients—play a significant role in the controller design. A body of work has shown that these coefficients shift with the propellers' operating regime. Both in the physics-based representations used in the advanced, realistic simulator reported in this paper [42] and in experimental studies, they are captured by multi-input relationships [44, 45] that are governed by propeller orientation, angular velocity, resultant airspeed, and geometric parameters.

The results documented in Section 6.2 were produced within a co-simulation setup that couples the physical Simcenter Amesim model—which embodies the UAV and its subsystem dynamics—with the hierarchical control algorithm implemented in Matlab Simulink. The approach followed in this paper, depicted conceptually in **Figure 4**, interfaces Matlab Simulink with the Simcenter environment via a dedicated connection.

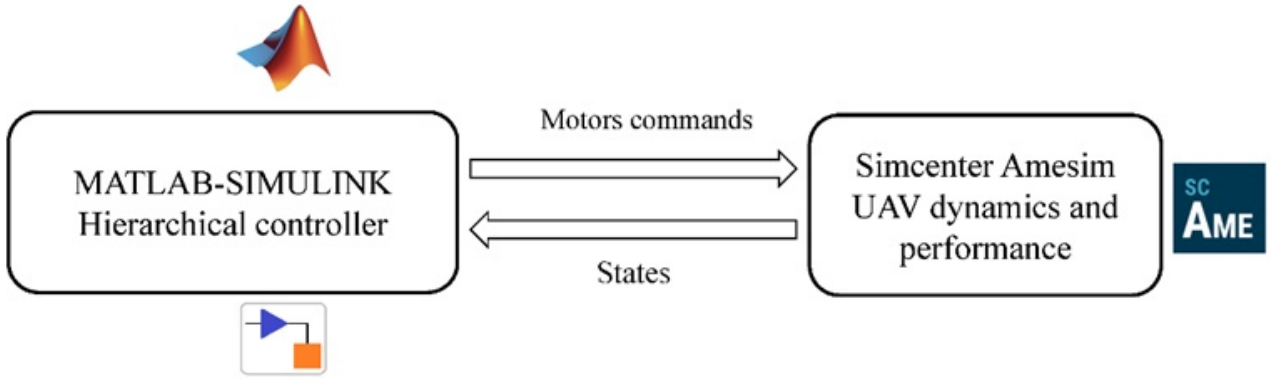

Figure 4. Optimal trajectory references for selected test simulations with terminal position states set to [663],[8610], [1785],[101010]: (a) Optimal position histories along the x-axis, (b) Optimal position histories along the y-axis, (c) Optimal

© 2023 The Author(s). | Published by Agro Intelligence Research Press

position histories along the z-axis, (d) Optimal velocity histories along the x-axis, (e) Optimal velocity histories along the y-axis, and (f) Optimal velocity histories along the z-axis.

For the present work, those parameters were identified under static assumptions during controller synthesis, even though they vary over time during the simulation. To offset this simplification and to harden the controller against uncertainty, variations in the propulsion level were also absorbed into the disturbance term.

The drone simulation parameters employed within the model-based design controller are summarized in **Table 1**.

Table 1. Nominal quadrotor parameters.

Symbol	Description	Value
m	Total mass of the UAV airframe	5 kg
l	Distance from the center of mass to the rotor shaft	0.3 m
J_1	Moment of inertia about the x-axis	0.011521 kg·m²
J_2	Moment of inertia about the y-axis	0.0362132 kg·m²
J_3	Moment of inertia about the z-axis	0.029142 kg·m²
J_p	Rotor (propeller) inertia	0.0003 kg·m²
g	Gravitational acceleration constant	9.81 m·s^{-2}
b	Thrust coefficient	4.5625 × 10^{-5} N·s²·rad^{-2}
c	Aerodynamic drag coefficient	1.375 × 10^{-5} N·s²·rad^{-2}·m

Simulation results in simulink and simcenter amesim co-simulation platform

For the test scenario reported here, we examined rest-to-rest translations of the Simcenter Amesim quadrotor, departing from the state [$xyz\psi$] = [0000] and aiming to reach [$xyz\psi$] = [102030π/4] as the target configuration. At both boundary points, the UAV was taken to possess vanishing linear and angular rates, with the body frame aligned to the inertial frame when t = 0. The gain settings employed by the controller throughout the displayed runs are catalogued in **Table 2**. The dominant waveforms that mark this simulation appear across **Figures 5-10**. **Figure 5** overlays the position commands and the measured Simcenter Amesim drone response, separately covering the x-direction (a) and the y-direction (b), while the companion subplots (c) and (d) plot the mismatch between the two. Owing to dynamics left out of the model and incomplete knowledge of certain coefficients, the discrepancy is not driven to zero but remains bounded.

© 2023 The Author(s). | Published by Agro Intelligence Research Press

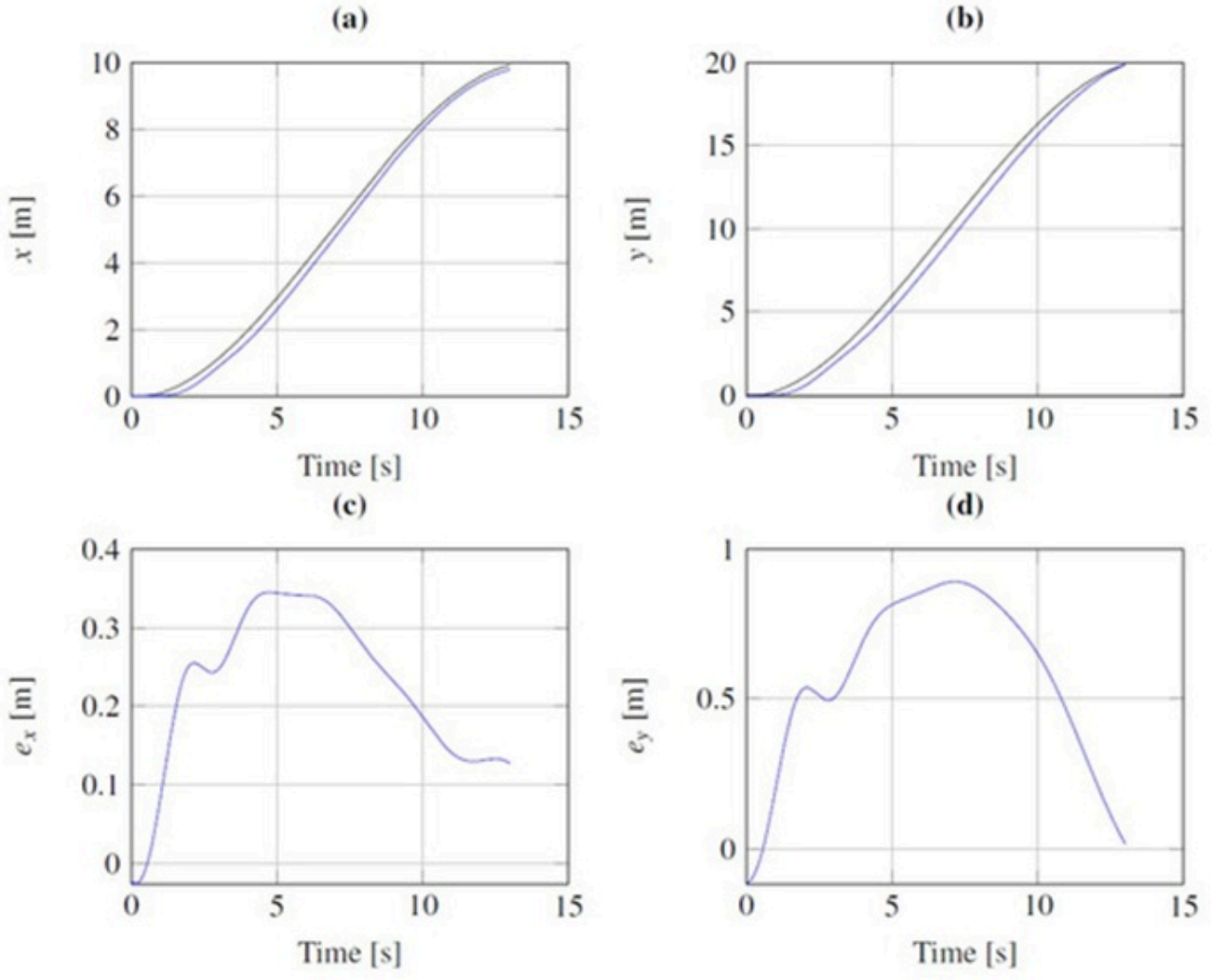

Figure 5. The co-simulation framework.

© 2023 The Author(s). | Published by Agro Intelligence Research Press

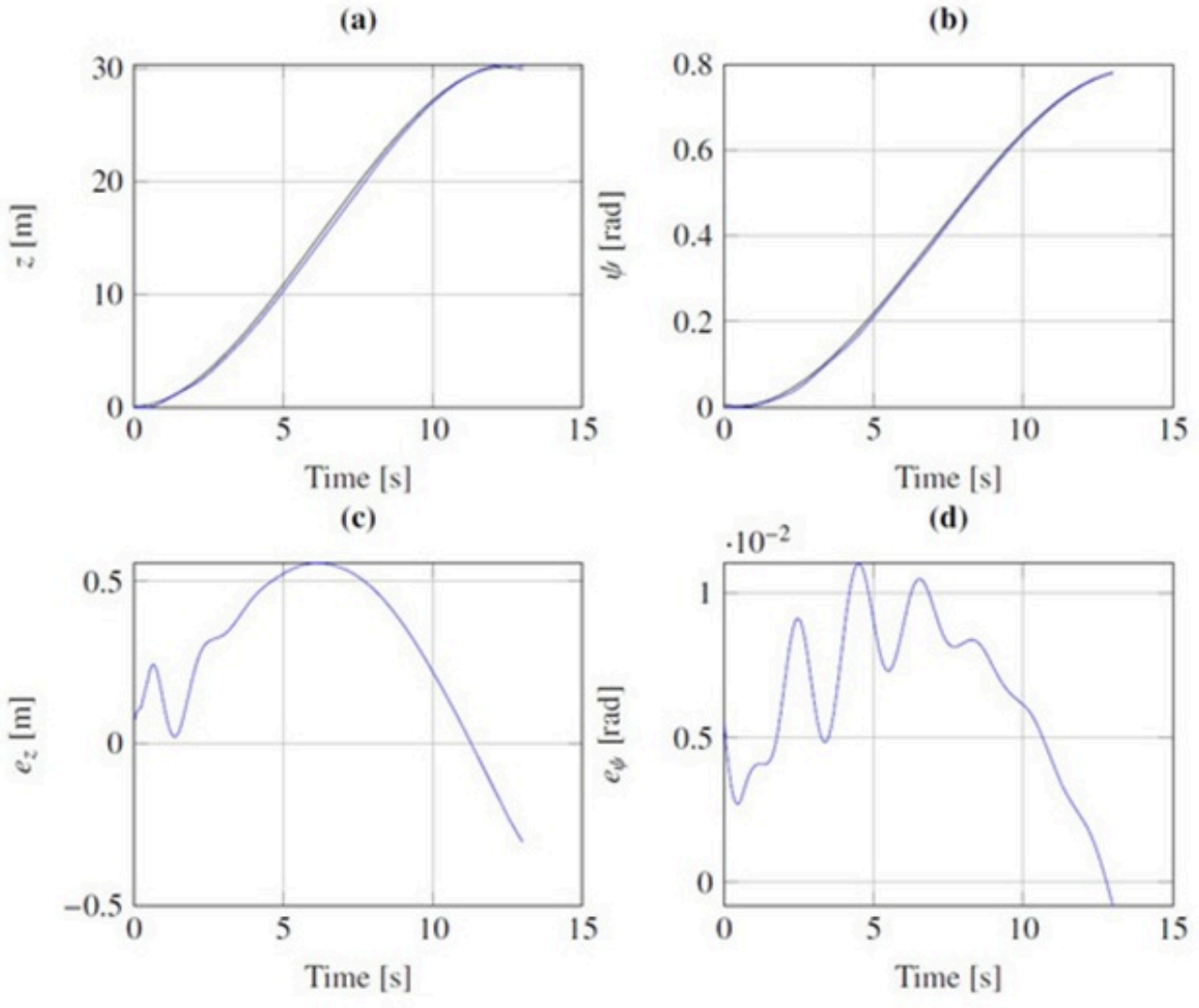

Figure 6. (a) Longitudinal UAV motion: command $xref$ (black trace) against controlled x (blue trace), (b) Latitudinal UAV motion: command $yref$ (black trace) against controlled y (blue trace), (c) Controlled UAV longitudinal error (x-axis), and (d) Controlled UAV latitudinal error (y-axis).

© 2023 The Author(s). | Published by Agro Intelligence Research Press

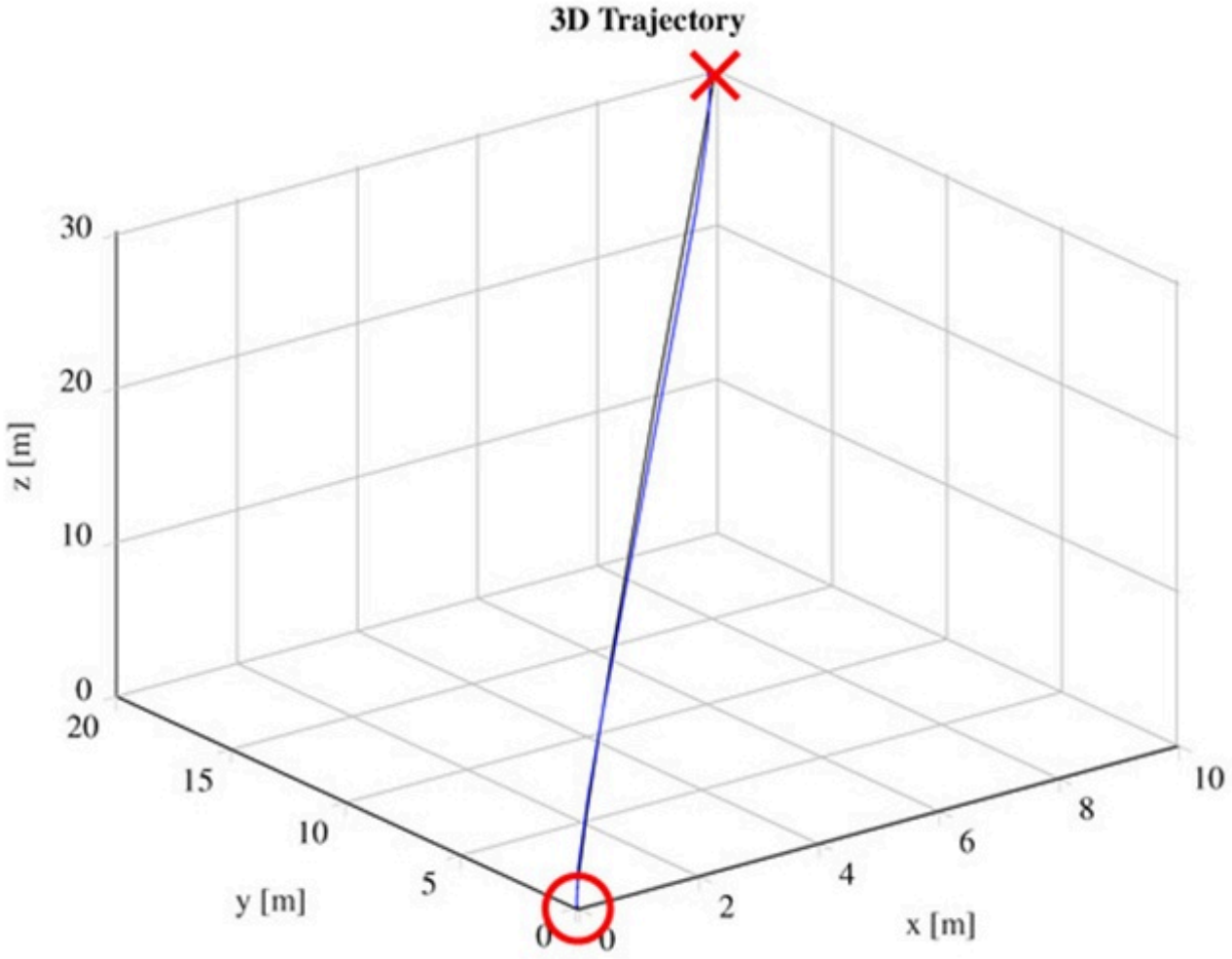

Figure 7. (a) Altitude evolution of the quadrotor: command $zref$ (black trace) against controlled z (blue trace), (b) Yaw angle of the quadrotor: command ψref (black trace) against controlled ψ (blue trace), (c) UAV altitude tracking error (z-axis), and (d) UAV yaw-angle tracking error.

© 2023 The Author(s). | Published by Agro Intelligence Research Press

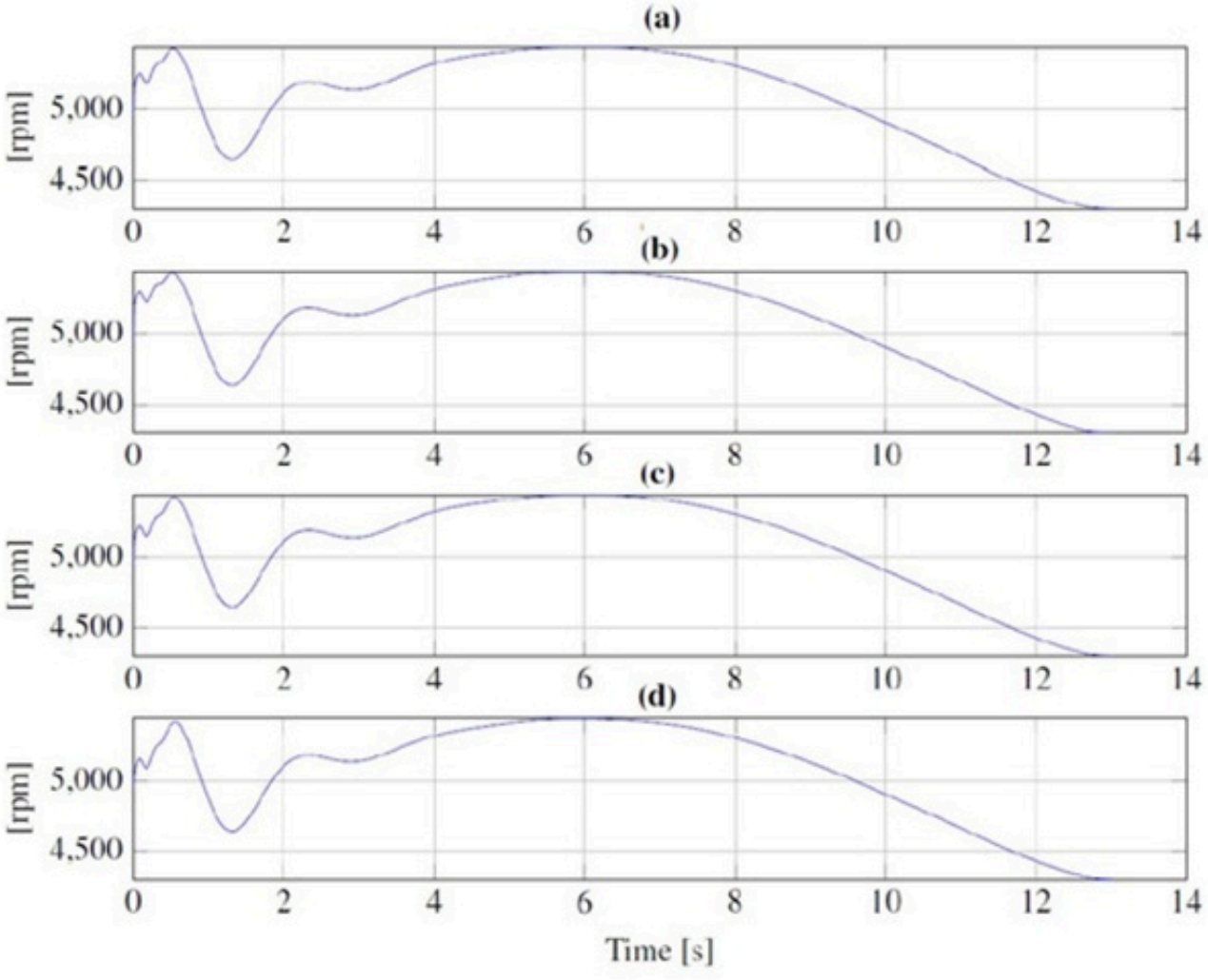

Figure 8. 3D flight path of the drone: command (black), robust control (blue). The circular marker and the cross marker pinpoint, in order, the initial and terminal points of the 3D reference path.

© 2023 The Author(s). | Published by Agro Intelligence Research Press

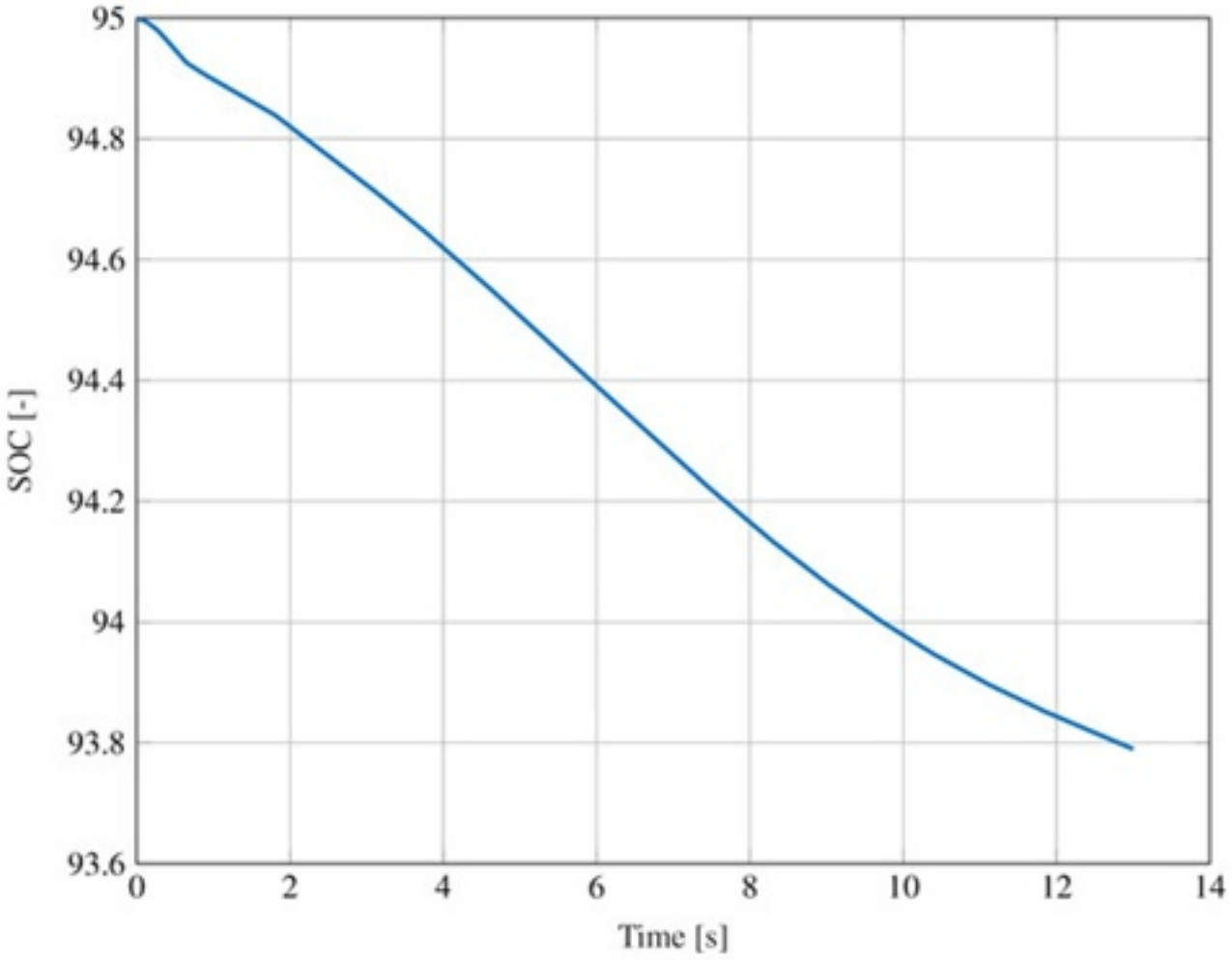

Figure 9. Propeller angular rates produced by the proposed controller: $\omega 1$ (a), $\omega 2$ (b), $\omega 3$ (c), $\omega 4$ (d).

© 2023 The Author(s). | Published by Agro Intelligence Research Press

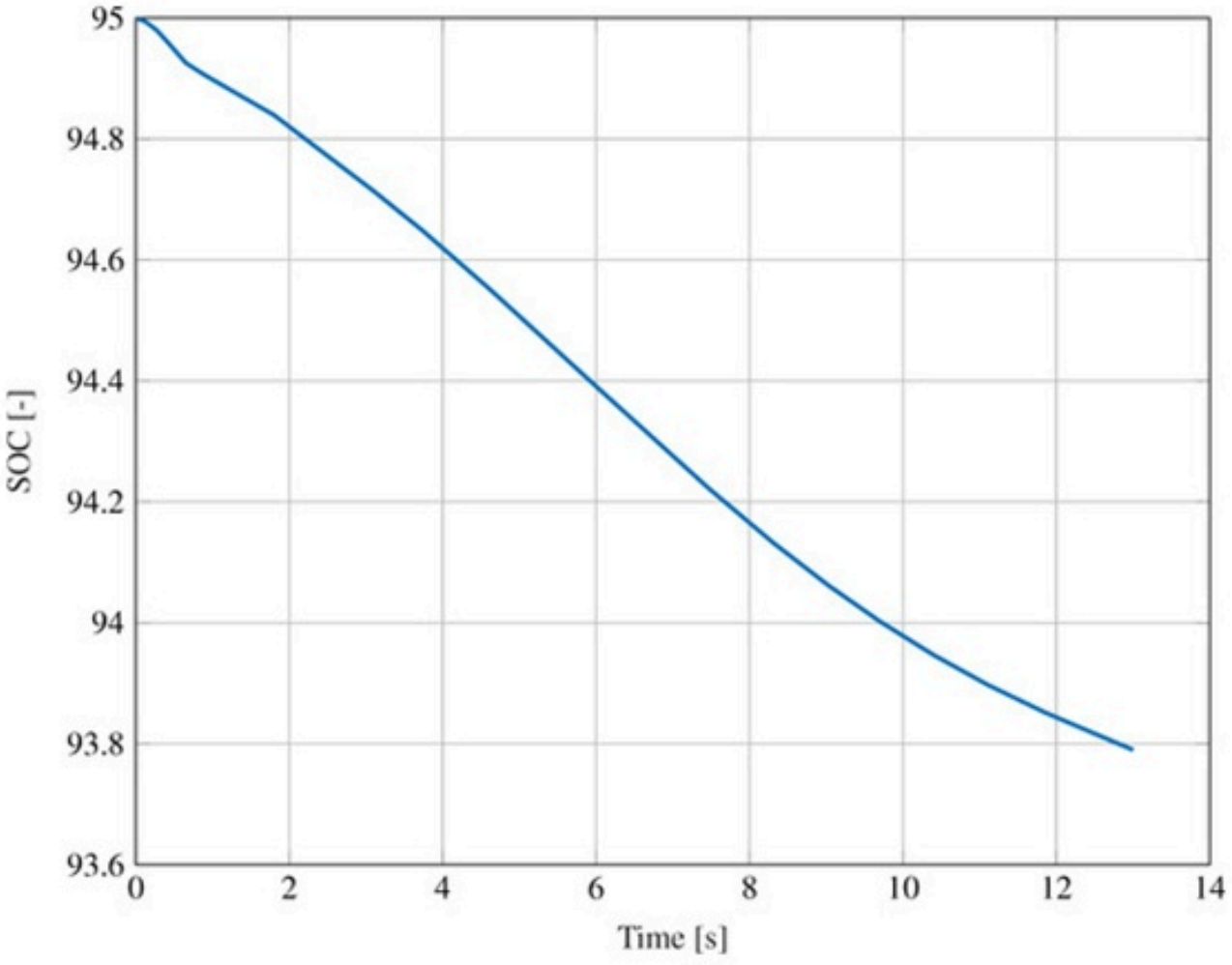

Figure 10. Battery SOC trend during the simulation run.

Table 2. Controller parameters.

kpx=kpy=4	kdx=kdy=1	kpz=50	kdz=5
$kp\theta$=$kp\phi$=$kp\psi$=5	$kd\theta$=0.5	$kd\phi$=0.5	$kd\psi$=0.5

What **Figure 6** portrays is the commanded alongside the actual drone altitude (a) and likewise for the yaw-angle channel (b). The lower panels (c) and (d) give the associated deviation signals, both of which remain small. Turning to the spatial reference path shown in **Figure 7**, the tracking quality is high, and the accumulated mismatch is practically insignificant relative to the richness of the plant model the controller is tasked with governing.

Figure 8 reports the rotational rates of the four propellers. None of these trajectories ever encroach upon the saturation threshold (fixed near 6.400 rpm), bearing out that the maneuver duration picked at the reference-generation layer following the procedure from Section 3 was well judged. **Figure 9** closes the sequence by charting the battery SOC: approximately 1.2% of the stored charge was drawn during this particular maneuver.

A three-way performance comparison is presented in **Table 3**, covering the optimal control (OC) baseline, the hierarchical controller paired with the simplified model (SM), and the hierarchical controller paired with the Simcenter Amesim model (AM). The metrics used are the cost functional J specified in **Eq. 8** and the terminal state of charge (SOC) recorded at the

© 2023 The Author(s). | Published by Agro Intelligence Research Press

end of each selected maneuver. Strikingly, the rule-based scheme augmented with hierarchical control stays tightly grouped with the optimal open-loop benchmark across both the energy and battery yardsticks. Equally noteworthy, the two performance figures remain closely matched regardless of whether the controller is exercised on the simplified or the Simcenter Amesim representation, suggesting that the adopted cost functional J indeed constitutes a faithful surrogate for actual battery drain. The proposed control structure stands out for its lean computational footprint. Thanks to its reliance on linear interpolation and elementary algebraic steps, it reaches a solution considerably faster than the optimal policy, which must invoke a numerical minimization routine. On the flip side, the optimal control formulation demands far less case-specific tuning and transfers more smoothly to fresh missions or to UAVs with altered specifications. This tension between computational swiftness and tuning flexibility captures the complementary virtues of the proposed control paradigm, rendering it adaptable to widely differing operational contexts and mission profiles.

Table 3. Comparison among optimal control (OC), SMC (simplified model control), and SAC (Simcenter Amesim control) operating alongside rule-based energetic reference generation for a range of heterogeneous missions. EC designates energy consumption, J. BC designates battery consumption.

	BC			EC J		
Final Point	**SAC**	**SMC**	**OC**	**SAC**	**SMC**	**OC**
[10,20,30]	101.27	101.31	100	101.43	101.52	100
[12,10,−40]	102.14	102.09	100	102.3	102.23	100
[8,10,6]	100.54	100.92	100	100.71	101.1	100
[−30,40,50]	101.78	102.11	100	101.9	102.3	100
[20,−20,−40]	101.95	102.21	102	102.02	102.17	100

Conclusion

The problem of steering a quadrotor through a mission while minimizing energy expenditure can be formalized and addressed within the optimal-control framework. Yet executing such a scheme in real time on board proves formidable, constrained as it is by tight computational and memory budgets. A rule-driven alternative, on the other hand, maps far more naturally onto online hardware, even if it comes at the cost of a painstaking calibration exercise. The path taken in this work consists of mining the decisions produced by the optimal-control formulation to unearth recurring patterns in optimal mission duration and reference shaping. The tunable degrees of freedom in the reference generator must be adjusted to ensure the rule-based waveforms closely match their optimal counterparts. The hierarchical controller crafted for this task faithfully shadows the reference paths and yields energy-consumption measures—both in terms of the cost functional embedded in the optimal control statement and in terms of actual battery depletion—that are very close to the optimal limit. It is worth noting that the reference generator and the optimal mission time are tailored to a specific UAV type and its characteristic parameters; any modification to those parameters requires a new design iteration. A worthwhile future inquiry could track how the optimal controller's chosen trajectories shift when the drone's physical properties, energy supply, or structural layout are varied. The performance claims for the proposed controller were substantiated through numerical trials, and side-by-side assessments were conducted covering path-following fidelity, an energy performance metric, and battery usage, using the Simcenter Amesim physical mock-up within a co-simulation loop with Matlab-Simulink. This end-to-end validation exercise offered meaningful evidence regarding the practical deployability and merit of the rule-based strategy in realistic UAV operational settings.

When considering follow-up work, a valuable extension would be to incorporate a disturbance observer into the control law, as described by Bianchi *et al.* [46]. The present study keeps its lens trained on the energetic and control dimensions inside a commercial simulation package, leaving aside external perturbations—most notably wind. The addition of a

© 2023 The Author(s). | Published by Agro Intelligence Research Press

disturbance estimator aims to strengthen the control action's robustness, thereby reducing errors arising from unmodeled effects and time-varying coefficients. Introducing this element is essential to maintaining the effectiveness and reliability of the control approach when transferred to real-world environments, where ambient factors can significantly influence UAV behavior.

Acknowledgements

The authors thank Siemens for the support in using Simcenter Amesim to best advantage during the European Project "COMP4DRONES", as the simulations were carried out during the project's validity period, which ended in January 2023. Furthermore, the authors are grateful to the editor and anonymous reviewers for their constructive comments and suggestions, which have improved this paper.

Conflict of interest

None

Financial support

This work was partially supported by the European Project ECSEL—Joint Undertaking RIA–2018 "Comp4Drones" under grant agreement No. 826610 and by the MAECI Project 2018–2020, "Coordination of autonomous unmanned vehicles for highly complex performances" PGR01083.

Ethics statement

None

Received: 04 Aug 2022 Revised: 09 Oct 2022 Accepted: 26 Oct 2022
Published online: 25 November 2023

Rights and permissions

Open Access The author(s) retain copyright. This article is licensed under the Creative Commons Attribution-NonCommercial-ShareAlike 4.0 International License. It may be shared and adapted for non-commercial purposes with appropriate attribution, an indication of changes, and distribution of adaptations under the same license. Third-party material may be subject to separate terms identified in its credit line. View the license at https://creativecommons.org/licenses/by-nc-sa/4.0/.

References

1. Mathews AJ, Singh K, Cummings AR, Rogers SR. Fundamental practices for drone remote sensing research across disciplines. Drone Syst Appl. 2023;11:1–22.

2. Santoso F, Garratt MA, Anavatti SG. State-of-the-art intelligent flight control systems in unmanned aerial vehicles. IEEE Trans Autom Sci Eng. 2018;15:613–27.

3. DDC: Drone Delivery Canada. https://dronedeliverycanada.com/ (accessed on 17 August 2023).

4. Wall Street Journal, Google Drones Can Already Deliver You Coffee In Australia. www.youtube.com/watch?v=prhDrfUgpB0 (accessed on 6 April 2019).

5. Zraick, K. Like ‘Uber for Organs’: Drone Delivers Kidney to Maryland Woman. The New York Times. www.nytimes.com/2019/04/30/health/drone-delivers-kidney.html (accessed on 17 August 2023).

6. Estevez J, Lopez-Guede JM, Grana M. Quasi-stationary state transportation of a hose with quadrotors. Robot Auton Syst. 2015;63:187–94.

7. Post S. Drones: A Vision Has Become Reality. http://www.swisspost.ch/drones (accessed on 17 August 2023).

8. Stolaroff JK, Samaras C, O’Neill ER, Lubers A, Mitchell AS, Ceperley D. Energy use and life cycle greenhouse gas emissions of drones for commercial package delivery. Nat Commun. 2018;9:409.

9. Jensen-Nau KR, Hermans T, Leang KK. Near-optimal area-coverage path planning of energy-constrained aerial robots with application in autonomous environmental monitoring. IEEE Trans Autom Sci Eng. 2021;18:1453–68.

10. Lin J, Wang Y, Miao Z, Wang H, Fierro R. Robust image-based landing control of a quadrotor on an unpredictable moving vehicle using circle features. IEEE Trans Autom Sci Eng. 2023;20:1429–40.

11. Bresciani T. Modelling, Identification and Control of a Quadrotor Helicopter. Master’s Thesis, Department of Automatic Control, Lund University, Lund, Sweden, 2008.

12. Swieringa KA, Hanson CB, Richardson JR, White JD, Hasan Z, Qian E, et al. Autonomous battery swapping system for small–scale helicopters. In: Proceedings of the 2010 IEEE International Conference on Robotics and Automation, Anchorage, AL, USA, 2010. p. 3335–40.

13. Leonard J, Savvaris A, Tsourdos A. Energy management in swarm of unmanned aerial vehicles. J Intell Robot Syst. 2014;74:233–50.

14. Junaid AB, Konoiko A, Zweiri Y, Sahinkaya M, Seneviratne L. Autonomous wireless selfcharging for multi-rotor unmanned aerial vehicles. Energies. 2017;10:803.

15. Campi T, Cruciani S, Feliziani M. Wireless power transfer technology applied to an autonomous electric UAV with a small secondary coil. Energies. 2018;11:352.

16. Kumar V, Michael N. Opportunities and challenges with autonomous micro aerial vehicles. Int J Robot Res. 2012;31:1279–91.

17. Abdilla A, Richards A, Burrow S. Power and endurance modelling of battery-powered rotorcraft. In: Proceedings of the IEEE International Conference on Intelligent Robots and Systems, Hamburg, Germany, 2015. p. 675–80.

18. Morton S, Papanikolopoulos N. A small hybrid ground-air vehicle concept. In: Proceedings of the IEEE/RSJ International Conference on Intelligent Robots and Systems (IROS), Vancouver, BC, Canada; 2017. p. 5149–54.

19. Economou J, Kladis G, Tsourdos A, White B. UAV optimum energy assignment using Dijkstra’s algorithm. In: Proceedings of the European Control Conference (ECC), Kos, Greece; 2007. p. 287–92.

20. Carvajal CP, Andaluz VH, Roberti F, Carelli R. Path-following control for aerial manipulators robots with priority on energy saving. Control Eng Pract. 2023;131:105401.

21. Mohiuddin A, Taha T, Zweiri Y, Gan D. Dual-UAV payload transportation using optimized velocity profiles via real-time dynamic programming. Drones. 2023;7:171.

© 2023 The Author(s). | Published by Agro Intelligence Research Press

22. Levermore T, Sahinkaya MN, Zweiri Y, Neaves B. Real-time velocity optimization to minimize energy use in passenger vehicles. Energies. 2017;10:30.

23. Rossi R, Santamaria-Navarro A, Andrade-Cetto J, Rocco P. Trajectory generation for unmanned aerial manipulators through quadratic programming. IEEE Robot Autom Lett. 2017;2:389–96.

24. Kreciglowa N, Karydis K, Kumar V. Energy efficiency of trajectory generation methods for stop-and-go aerial robot navigation. In: Proceedings of the International Conference on Unmanned Aircraft Systems (ICUAS), Miami, FL, USA; 2017. p. 656–62.

25. Jacewicz M, Zugaj M, Glebocki R, Bibik P. Quadrotor model for energy consumption analysis. Energies. 2022;15:7136.

26. Chodnicki M, Siemiatkowska B, Stecz W, Stepien S. Energy efficient UAV flight control method in an environment with obstacles and gusts of wind. Energies. 2022;15:3730.

27. Morbidi F, Cano R, Lara D. Minimum-energy path generation for a quadrotor UAV. In: Proceedings of the IEEE International Conference on Robotics and Automation (ICRA), Stockholm, Sweden; 2016. p. 1492–8.

28. Zhou H, Xiong HL, Liu Y, Tan ND, Chen L. Trajectory planning algorithm of UAV based on system positioning accuracy constraints. Electronics. 2020;9:250.

29. Yu G, Cabecinhas D, Cunha R, Silvestre C. Quadrotor trajectory generation and tracking for aggressive maneuvers with attitude constraints. IFAC-PapersOnLine. 2019;52:55–60.

30. Schacht-Rodriguez R, Ponsart JC, Garcia-Beltran CD, Astorga-Zaragoza CM, Theilliol D, Zhang Y. Path planning generation algorithm for a class of UAV multirotor based on state of health of lithium polymer battery. J Intell Robot Syst. 2018;91:115–31.

31. Wu M, Chen W, Tian X. Optimal energy consumption path planning for quadrotor uav transmission tower inspection based on simulated annealing algorithm. Energies. 2022;15:8036.

32. Jiang B, Li B, Zhou W, Lo LY, Chen CK, Wen CY. Neural network based model predictive control for a quadrotor UAV. Aerospace. 2022;9:460.

33. Giernacki W. minimum energy control of quadrotor uav: synthesis and performance analysis of control system with neurobiologically inspired intelligent controller (BELBIC). Energies. 2022;15:7566.

34. Bianchi D, Rolando L, Serrao L, Onori S, Rizzoni G, Al-Khayat N, et al. Layered control strategies for hybrid electric vehicles based on optimal control. Int J Electr Hybrid Veh. 2011;3:191–217.

35. Gieras JF. Permanent Magnet Motor Technology: Design and Applications; CRC Press, Taylor and Francis Group: Boca Raton, FL, USA, 2009.

36. Bouabdallah S, Murrieri P, Siegwart R. Towards autonomous indoor micro VTOL. Auton Robot. 2005;18:171–83.

37. Carrillo LR, Lopez AE, Lozano R, Pegard C. Quad Rotorcraft Control: Vision-Based Hovering and Navigation; Springer: London, UK, 2013.

38. Lua CA, Garcia CCV, Di Gennaro S, Castillo–Toledo B, Morales MES. Real–time hovering control of unmanned aerial vehicles. Math Probl Eng. 2020;2020:2314356.

39. Mendoza LFM, Bonilla JTG, Garcia-Torales G, Lua CA, Di Gennaro S. Visual Sensor System Applied to Trajectory Generation for UAVs. In: Proceedings of the IEEE International Autumn Meeting on Power, Electronics and Computing (ROPEC), Ixtapa, Mexico; 2022.

© 2023 The Author(s). | Published by Agro Intelligence Research Press

40. Li YR, Peng CC. Development of a full orientation flight robotics: Dynamics modeling, analysis, and control design. IEEE Access. 2023;11:110234–44.

41. Jongerden MR, Haverkort BR. Which battery model to use? IET Softw. 2012;3:445–57.

42. Cappuzzo F, Dezobry V, Bianchi D, Di Gennaro S. A Novel Co-simulation Framework for Verification and Validation of GNC Algorithms for Autonomous UAV. In: Proceedings of the Vertical Flight Society's 78th Annual Forum & Technology Display, Fort Worth, TX, USA; 2022.

43. Siemens: Simcenter Amesim 2021.1 Reference Guide 2021. https://docs.plm.automation.siemens.com/content/amesim/17/help/en_US/quick_start_guide/references.html (accessed on 19 January 2024).

44. Nguyen DH, Liu Y, Mori K. Experimental study for aerodynamic performance of quadrotor helicopter. Trans Jpn Soc Aeronaut Space Sci. 2018;61:29–39.

45. Six D, Briot S, Erskine J, Chriette A. Identification of the propeller coefficients and dynamic parameters of a hovering quadrotor from flight data. IEEE Robot Autom Lett. 2020;5:1063–70.

46. Bianchi D, Di Gennaro S, Di Ferdinando MD, Lua CA. Robust control of UAV with disturbances and uncertainty estimation. Machines. 2023;11:352.

© 2023 The Author(s). | Published by Agro Intelligence Research Press